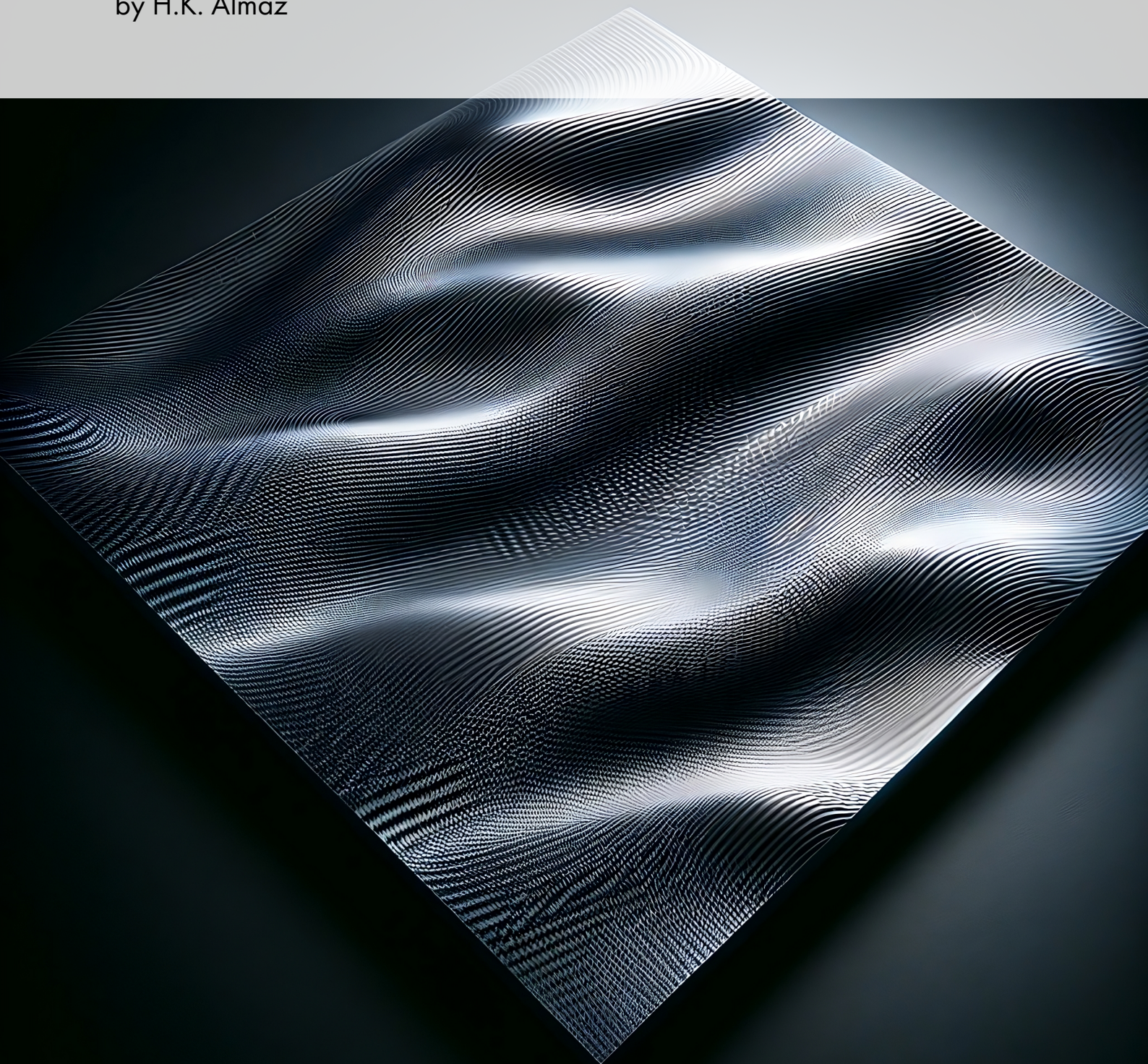


Post-buckling analysis of composite stiffened panels

A systematic analysis on the influence of imperfections

by H.K. Almaz



Post-buckling analysis of composite stiffened panels

A systematic analysis on the influence of imperfections

Thesis report

by

H.K. Almaz

to obtain the degree of Master of Science
at the Delft University of Technology
to be defended publicly on January 19, 2024 at 12:30

Thesis committee:

Chair: Prof. Dr. C. (Christos) Kassapoglou
Supervisor: Dr.ing. S. (Saullo) Giovanni Pereira Castro
External examiner: Dr. N. (Nan) Yue
Place: Faculty of Aerospace Engineering, Delft
Project Duration: June, 2023 - January, 2024
Student number: 4807073

An electronic version of this thesis is available at <http://repository.tudelft.nl/>.

Cover: AI art made using DALL-E representing an abstract buckled panel



Copyright © H.K. Almaz, 2024
All rights reserved.

Abstract

Pushing the envelope of aerospace structures requires the complete exploitation of their potential in terms of load-carrying capacity per unit weight for both economic and ecological reasons: the two most important being the reduction of fuel consumption and greenhouse gas emissions. A key approach involves allowing structures like stiffened panels to function within the post-buckling range domain while in service. To do so, the finite element approach allows a broad design space for researching the post-buckling behaviour of such structures.

Accurately representing post-buckling behaviour in finite element models requires accounting for geometric and loading imperfections. The present study explores their effects on the post-buckling behaviour of a composite L-stiffened panel. A finite element model is created and validated based on an experimental case. This is then further modified to incorporate imperfections. Geometric imperfections are modelled using linear eigenvalue modes, while loading imperfections are introduced via a rigid loading plate making contact at an angle.

The research showed that both first and higher eigenmode combinations for geometric imperfections influence post-buckling behaviour. Their shape and amplitude impact the transition into post-buckling and their ultimate loads. Similar behaviour was also observed for loading imperfections. Additionally, their configuration also showed an offset in axial displacement results. These insights emphasise the need for precise imperfection modelling to promote safer and more efficient post-buckling design of aerospace structures.

Contents

Abstract	iii
1 Introduction	1
1.1 Literature Review	2
1.1.1 Analytical Models	2
1.1.2 Finite Element Models	3
1.1.3 Concluding Remarks	10
1.2 Research Objective	10
1.3 Thesis Outline	11
2 Baseline Model	12
2.1 Reference Case	12
2.2 Finite Element Implementation	13
2.2.1 Boundary Conditions	14
2.2.2 Analysis Methods	16
2.3 Validation	17
3 Imperfection Modelling	24
3.1 Geometric Imperfection	24
3.1.1 Modelling	25
3.1.2 Observations	26
3.2 Loading Imperfection	32
3.2.1 Modelling	33
3.2.2 Observations	34
3.3 Remarks	35
4 Results and Discussion	36
4.1 Results Lanzi case	36
4.2 Results Geometric Imperfections	38
4.3 Results Loading Imperfections	42
4.4 Discussion	45
5 Conclusion	47
5.1 Reflection on Research Questions	47
5.2 Concluding Remarks	49
6 Recommendations	50
References	55
A Baseline Configurations	56

B Additional Imperfection Data

60

C Additonal Data

62

*"Like my panels, my life is a canvas of imperfections,
each flaw painting a unique and non-linear story."*

- H.K. Almaz

Introduction

The aerospace industry has been experiencing rapid growth, and so have their greenhouse gas emissions. In 2022, the aerospace sector was responsible for 2% of global carbon dioxide (CO₂) emissions¹. Given the swift expansion of the industry, there is a pressing need for action within aerospace companies to reduce their ecological footprint. The International Civil Aviation Organisation (ICAO) agreed on a long-term goal of achieving net-zero CO₂ emission by 2050 [1]. One of the challenges that has to be overcome to achieve this goal is exploiting structures to their fullest potential. Enabling this will result in lighter, more economic designs, reduced fuel consumption, and ultimately lower emissions. To pursue these goals, new design scenarios are being explored. An example is the European CO-COMAT project, which was initiated to investigate the effects of reducing structural weight by allowing stiffened panels to undergo post-buckling. Buckling is defined as the sudden or gradual change in shape of a structure at a critical load. Hence, post-buckling refers to the non-linear behaviour after this point. Stiffened panels, commonly found in aircraft wing box designs, effectively enable the structures to handle increased loads without adding excessive weight. Upon buckling, the stiffness of a stiffened panel's skin decreases, and the stiffeners assume a more significant role in bearing the redistributed loads. Therefore, to fully realise the potential of these designs, it is essential to understand their post-buckling behaviour. By allowing post-buckling, one extends the failure or stability limit of the structure. Extending the structure's limit permits designs with less reinforcement for the same load case, resulting in lighter and more environmentally friendly designs. For stiffened composite panels, the shift in approach from the current design scenario to a future approach is illustrated in Figure 1.1.

¹<https://www.icao.int/environmental-protection/pages/aircraft-engine-emissions.aspx>

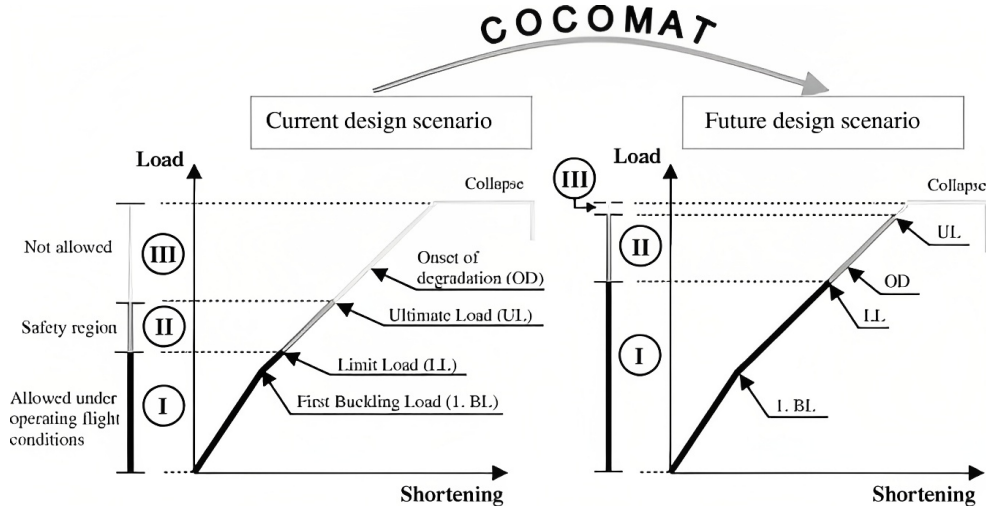


Figure 1.1: Current and future design scenarios for typical stiffened composite panel (Figure Courtesy: [2]).

The following sections provide a comprehensive overview of existing research on analysing the post-buckling behaviour of stiffened panels. The primary focus will be on examining the influence of imperfections, which mainly arise from manufacturing errors or variations in material properties. It is crucial to consider these irregularities to comprehend post-buckling behaviour accurately.

1.1 Literature Review

The review considers analytical and finite element (FE) models, with more priority on the latter, as they stand out in their ability to model physical principles for more complex geometries. Given the high costs associated with experimental work, particularly during the preliminary design stages of a design process [3, 4], they will be only discussed in the context of validating the FE models. Once validated with experimental data, FE models are more cost-effective and allow for the exploration of a broader design space.

1.1.1 Analytical Models

One of the works on post-buckling has been presented by Romeo et al. [5]. They formulated a closed-form solution for the out-of-plane displacement of the skin between consecutive stiffeners of a straight composite panel. Because of the limited availability of experimental data in the field at the time of publication in 1997, an experiment was conducted to validate the analytical predictions and assess the accuracy of the proposed model. Unstiffened and blade-stiffened panels², with simply supported boundary conditions, were subjected to biaxial compression ($N_y = 40\% N_x$) in the test. Figure 1.2 presents the results obtained for the analytical and experimental work in the case of an unstiffened panel to compare the skin behaviour. The analytical results are categorised into outcomes from load control (L.C.) and displacement control (D.C.) tests for both perfect and geometrically imperfect models. One of the observations is that the case with D.C., including imperfections, shows

²A blade stiffener is a stiffener attached perpendicular to the panel, featuring horizontal flanges on both sides that are connected to the panel skin.

better agreement with the experimental results (see left graph). The right graph illustrates the out-of-plane displacement across the panel's mid-length at an applied longitudinal load of 186 kN, again with better agreement for the D.C.-based results. The analytical models could not predict the post-buckling behaviour because the ultimate load was reached before non-linear behaviour was expected. Therefore, it was not realistic to compare the analytical predictions with the experimental results for the stiffened panel, which had an ultimate load twice that of its buckling load since the stiffeners continued carrying the load after buckling. [5]

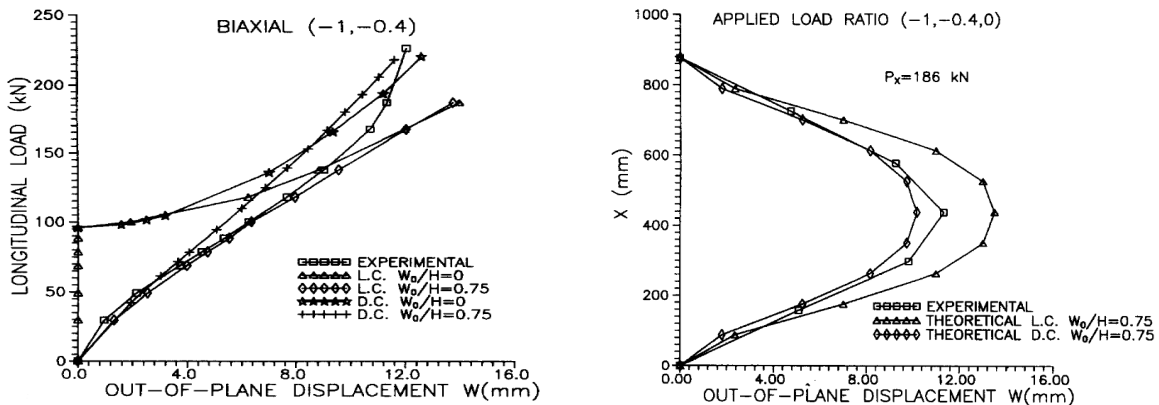


Figure 1.2: Experimental and analytical results with initial imperfections: Out-of-plane displacement curves versus applied longitudinal load (left) and out-of-plane displacement across the panel mid-length at an applied longitudinal load of 186 kN (right) (Figure Courtesy: [5]).

Vescovini et al. [6] and Schilling et al. [3] also formulated analytical expressions applied to stringer-stiffened single panels. Similarly, Mittelstedt et al. [7], Chandra [8] and Beerhorst et al. [9] focused on single panels. The differences in those research studies lie in, amongst other details, the type of boundary conditions and loads applied. Many of these analytical models show remarkable computational efficiency. However, a major limitation arises in their applicability, especially concerning more complex structures and the presence of discontinuities such as cut-outs. Only a few studies have considered multiple panel assemblies for their analytical tools, such as the work by Milazzo et al. [10] and Castro et al. [11], both focussing on dividing the main domain into subdomains.

1.1.2 Finite Element Models

Typically, when the geometry being analysed becomes complex or discontinuous, the geometries are approximated with a more general approach based on simpler entities. The finite element method (FEM) is amongst the most popular tools for analysing mechanical problems. One of the advantages is its capability to handle complex geometries and boundary conditions that are difficult to model analytically. FEM is extensively applied to predict the post-buckling behaviour of stiffened panels [12–16]. This increased fidelity comes at the cost of increased computational expense. However, this can be reduced by selecting more suitable parameters, such as the mesh size, without affecting the relevant results for a particular case.

In the context of post-buckling, some papers have explicitly discussed the influence of geo-

metric imperfections and the methods employed to implement them in FE models. Arbelo et al. [13] analysed the effect of imperfections on the post-buckling behaviour of stiffened panels. The work analysed composite panels subjected to in-plane shear loading, also considering imperfections resulting from the geometric and material nonlinearities. Good agreement was achieved upon comparing the numerical results obtained from the commercial solver ABAQUS with the experimental data (Figure 1.3). Mid-plane imperfections of the skin seemed to have minimal impact on the post-buckling behaviour. However, an evident offset was noted in the out-of-plane displacement between the experimental and numerical results. This was attributed to the clearance within the loading frame of the test device.

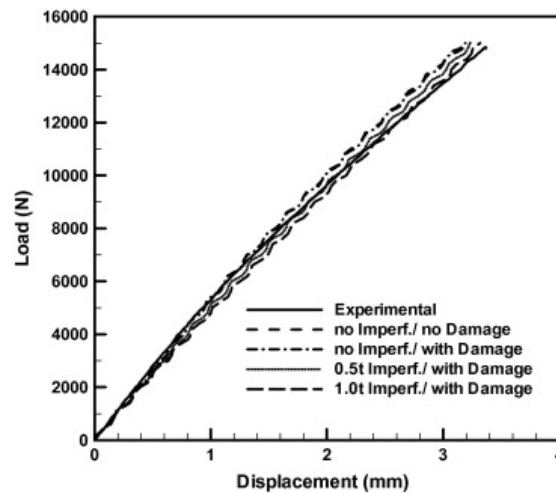


Figure 1.3: Comparison of the load with respect to displacement for the numerical and experimental results (Figure Courtesy: [13]).

Lynch et al. [14] investigated the behaviour of stringer-stiffened panels subjected to compression loads in fuselage structures. The analysis of post-buckling behaviour was carried out using ABAQUS and the Newton-Raphson method. Although the conventional Newton-Raphson method demonstrates good convergence rates [17], it may fail to converge when sudden non-linear behaviour is observed in a structure, such as load drops. To mitigate this problem, artificial damping was introduced in the non-linear solver, where artificial viscous forces are created to dissipate the energy of local instabilities. The imperfection was included using the buckling mode shape. This method imposes a mode from an eigenvalue analysis as an initial state of the model geometry, whose amplitude is scaled using a scaling factor. The maximum scaling factor for the imperfection amplitude equals 10% of the skin thickness, a typical value for riveted structures [14]. The ultimate loads obtained (Figure 1.4) revealed a high sensitivity to overall imperfections. The presence of the imperfections led to higher out-of-plane displacements with increasing compression loads and, ultimately, lower failure load: Figure 1.4 shows the clear difference in failure load with the increase of imperfection magnitude. Although the imperfections are present in the specimen, they do not occur in the actual fuselage structure because of the presence of frames in the latter case. The frames prevent the deflection of the stiffeners, and the only possible deflection occurring in the skin is in between the stiffeners, proving that incorporating such imperfections is still essential for more accurate and representative models. To create better agreement with the

experiments, Lynch et al. recommended the inclusion of residual stresses resulting from riveting.

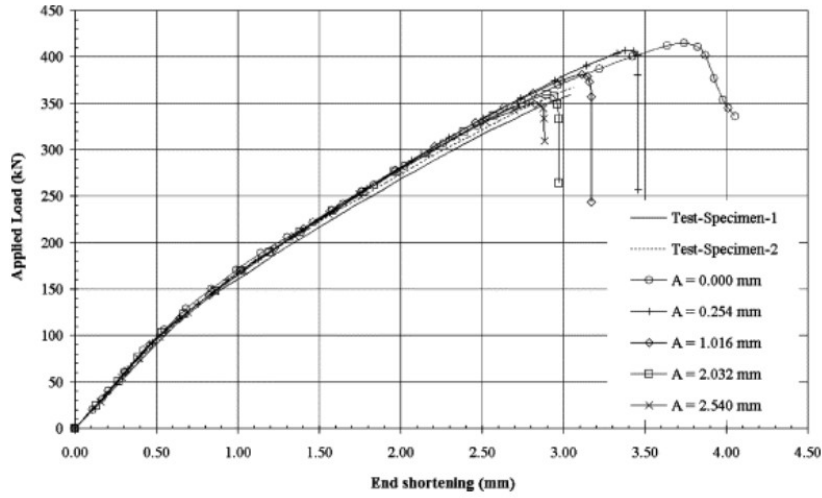


Figure 1.4: Different lines representing the load versus axial shortening of two test specimens and the numerical models with and without imperfections (Figure Courtesy: [14]).

The inclusion of buckling mode shapes from eigenvalue analysis, as demonstrated by Lynch et al., is a commonly employed method to account for geometric imperfections. This approach is also underscored in the paper by Castro et al. [18] and the review by Farzarian et al. [19]. Schafer and Pekoz [20] propose a modelling strategy to address geometric imperfections, recommending the combination of at least two modes with distinct shapes. Their study provides an example where the inclusion of only one mode yields to be less conservative, emphasising the necessity of combining appropriate modes to generate an accurate geometric pattern compared to measured imperfections. The amplitude of the imperfection is determined by applying one of the approximate formulas expressed in Equation 1.1 [20]: The maximum amplitude α is formulated in terms of panel width w or thickness t in mm (for $w/t < 200$). These equations are derived using simple rules of thumb and probabilistic analyses. The reader is referred to the paper [20] for the complete explanation.

$$\begin{aligned}\alpha &\approx 0.006w \\ \alpha &\approx 6te^{-2t}\end{aligned}\tag{1.1}$$

Following a similar train of thought, Gardner [21] focused only on the first two modes. However, here the amplitude was determined by measured imperfection values and empirical equations. Upon comparing with experimental test results, the empirical equation showed the best agreement, see Equation 1.2 [21]. The constant γ in the expression is usually determined experimentally, but Dawson and Walker suggest $\gamma = 0.2$ as the most suitable factor for determining the amplitude. The yield stress σ_y and critical buckling stress σ_{cr} are based on the material properties.

$$\alpha = \gamma (\sigma_y / \sigma_{cr}) t\tag{1.2}$$

Bisagni and Dávila [22] consider linear combinations of the first three buckling modes from the linear eigenvalue analysis and scaling these to an amplitude of 1% of the skin thickness. This amplitude was selected to align the outcomes of numerical analyses with the experimental data through curve fitting.

Continuing on the review on stiffened panels, Ambur et al. [23] add measured geometric and thickness imperfections in their model. The latter results from uneven thickness distribution over the skin. The inclusion of the imperfections produced load-displacement values similar to those obtained from the experiments. However, there is no elaboration on how these imperfections influence the post-buckled shape and the ultimate loads of the structure.

Numerical analysis performed by Orifici et al. [24] included measured geometric imperfections in the skin of the blade-stiffened panels. The primary distinction was observed during the shift from local skin buckling to global buckling, where the stiffeners mainly carry the load in global buckling. The observed modes from the experiments were captured well in the numerical model using ABAQUS (see Figure 1.5), except for the modes with asymmetric behaviour. This is due to the shape changes at an edge caused by the manufacturing and curing process. In addition to this, because of the absence of longitudinal edge supports, the geometric imperfections are likely to influence the buckling shapes directly [24].

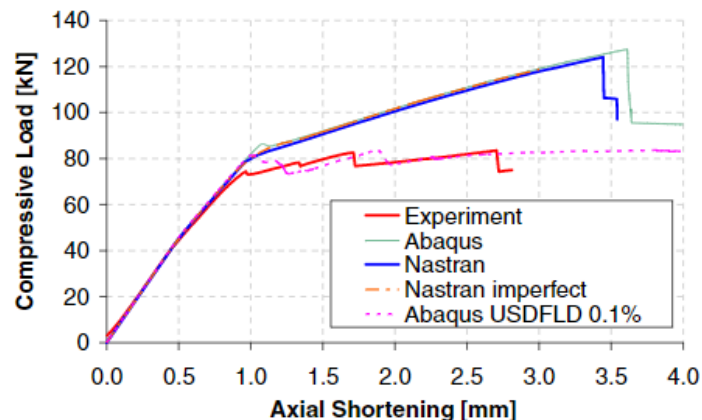


Figure 1.5: A comparison between the load-shortening behaviour of a structure as observed through experimental testing and as predicted by numerical simulations (Figure Courtesy: [24]).

In the more recent work of Steltner et al. [12], an approach is presented for optimising the thickness of curved stiffened panels subjected to geometric imperfections. The perfect and imperfect panel results are shown in Figure 1.6. Comparing Figure 1.6(b) and (c) show skin sensitivity to imperfections. The perfect panel reaches the global buckling at a displacement (u_p) ~ 1.5 mm (Figure 1.6b - middle plot), and the imperfect panel at ~ 1.1 mm (Figure 1.6c - middle plot). The third plot in Figure 1.6b and Figure 1.6c show the post-buckling behaviour. In the case of the imperfect panel, the second decrease in reaction force happens at approximately $u_p \sim 1.3$ mm, corresponding to the formation of a post-buckled shape [12]. In the remaining part of the study, the imperfect panel is regarded as the initial case due to the substantial influence of imperfections on both buckling behaviour and load-carrying capacity.

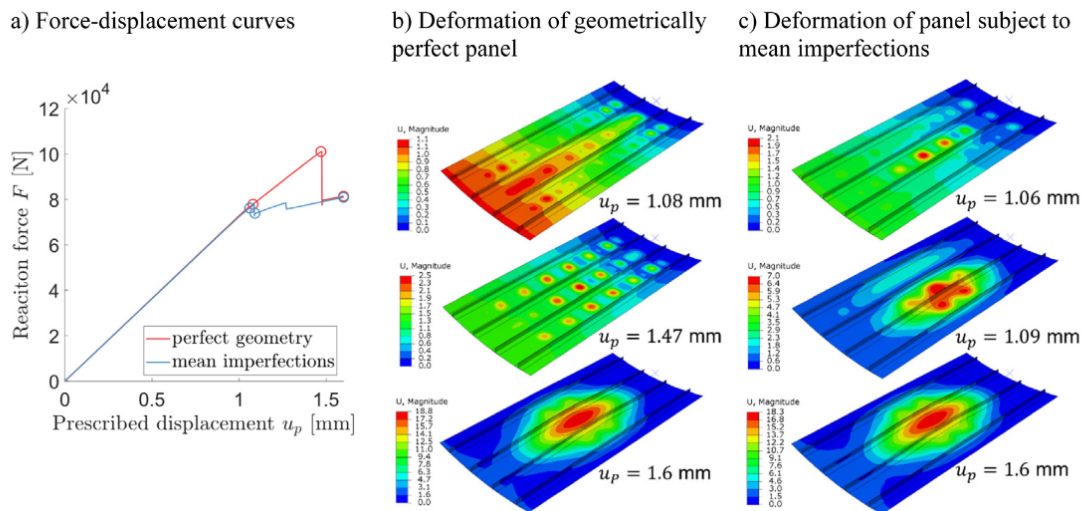


Figure 1.6: Force–displacement curves and visualisations of initial buckling mode up to final post-buckling mode (Figure Courtesy: [12]).

Prato et al. [15] also consider the combined effect of joints and geometric imperfections in their study of L-stiffened aluminium panels. In the experiments, the stiffeners were joined using a thin layer of adhesive and rivets. In FEM, two types of models are created: In the first one, the components are modelled out of one part, whereby the stiffeners and panel are integrated (single-component model). For the second, they are modelled separately (multi-component model) and include the joint. The rivets, in this case, are modelled using discrete node-based elements, see Figure 1.7, and their masses are included in the form of point loads. The adhesive was initially modelled using cohesive elements. However, their effect was negligible in the force-displacement curve compared to the rivets, so they were not considered at the end.

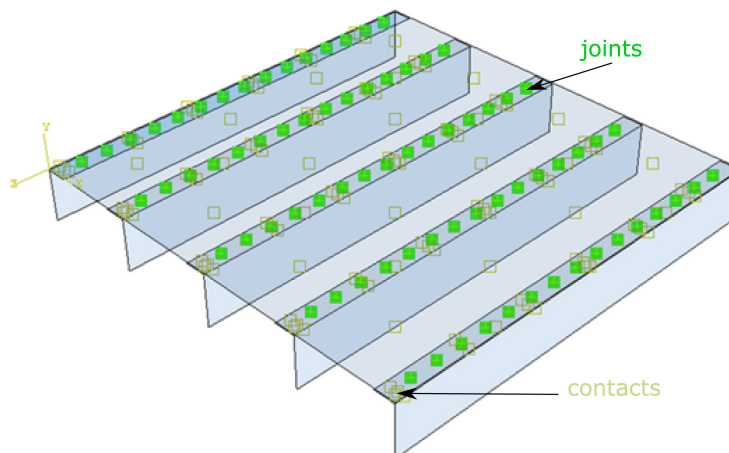


Figure 1.7: The inclusion of the rivets as discrete joints in the imperfect FE model (Figure Courtesy: [15]).

Figure 1.8 compares the experimental results and the multiple-component FE models by Prato et al. [15]. The perfect 'benchmark' model is compared with different models with imperfections. The in-plane imperfections, due to different stiffeners and panel lengths, are

introduced based on measurements from the experiments. The out-of-plane imperfections, on the other hand, were introduced by imposing the modes from the linear eigenvalue analysis. The figure presents the results of the models where in- and out-of-plane imperfections are included for specific stiffeners, and the 'all-imp.' model includes all the imperfections.

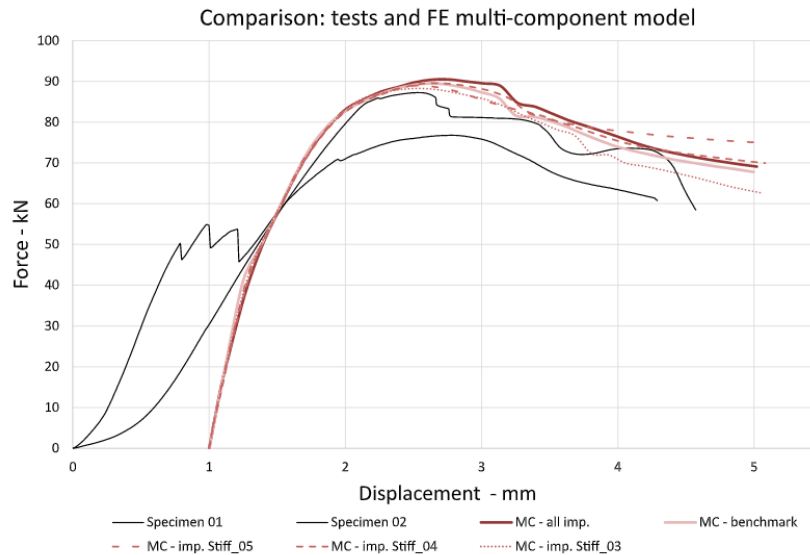


Figure 1.8: Comparison of the multi-component 'benchmark' model including joint imperfection with varying geometric imperfections using experimental testing and finite element modelling (Figure Courtesy: [15]).

Around the buckling load, minor differences are noticeable between the models for different imperfections. But their difference increases in the post-buckling region. Comparing the single-component and multi-component models, Prato et al. state that both models demonstrated sensitivity to geometric imperfections in the post-buckling region. They also noted that incorporating the joints increased the correspondence between the FE models and the experimental results. To improve the modelling of the joints, the authors recommend adding plasticity and a failure criterion. Albeit at the expense of increased computational cost.

Up to this point, geometric imperfections have predominantly been accounted for in numerical predictions. Nevertheless, there remains a gap in studying the effects of alternative types of imperfections. Stiffened panel studies have rarely addressed imperfections resulting from unevenly distributed loading - referred to as loading imperfections from now on - despite the intended uniformity of the load. So far, in all the aforementioned literature models, the loads were considered to be evenly distributed. One of the recent papers addressing the possible influence of loading imperfections is the research presented by van Dooren et al. [25]. They developed a numerical and experimental model for the skin stiffener separation of thermoplastic welded panels. According to the authors, the observed differences between the experimental and numerical results were possibly caused by loading imperfections. These imperfections stemmed from the lack of perfect flatness and alignment in both the machine's loading plate and the panel's loading surface.

To the author's knowledge, the only research found to include loading imperfections for composite stiffened panels is the work of Park et al. [26]. In their paper, they discuss the

design proposed by Nagendra et al. [27], blade-stiffened composite panels loaded in axial compression. These panels were manufactured and tested by NASA. The major difference between the design and test data was the out-of-plane displacement. Hence, the objective of Park et al. is to improve the correlation between these outcomes in their study. One approach in the numerical study of Park et al. was tilting the loading plate at a certain angle to introduce loading imperfections. A range between 0.005 and 0.01 degrees was considered for the tilt angle. See Figure 1.9 for the schematic overview [26].

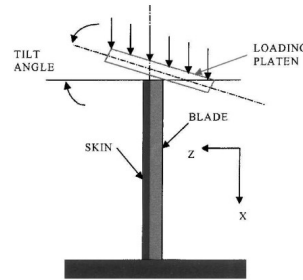


Figure 1.9: Overview of the side view of the blade stiffened panel with the loading plate and tilt angle (Figure Courtesy: [26]).

This approach resulted in similar out-of-plane and in-plane patterns as observed in the experiments. In Figure 1.10, the test data is compared with numerical models with different tilt angles. Among them, Model 9, with a tilt angle of 0.01 degrees, exhibited the most favourable response. Nevertheless, it demonstrated a comparatively lower overall offset.

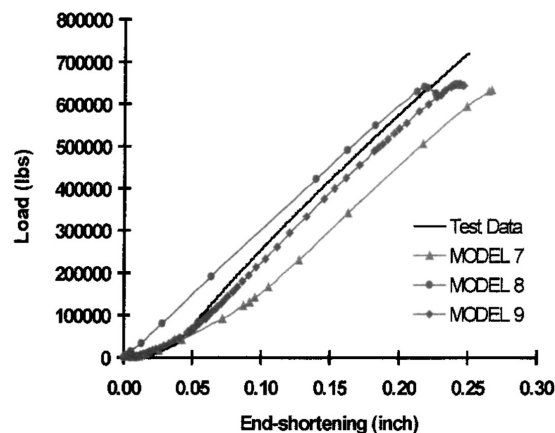


Figure 1.10: Load versus shortening curve for test- and numerical data (Figure Courtesy: [26]).

Park et al. [26] tilt-angle approach was adapted from the study of Hilburger [26, 28]. They investigated compression-loaded cylindrical shells with cutouts. This study modelled loading imperfections in two different ways: one already mentioned, the tilted loading plate, which usually occurs at the start of the experiment and causes a tilted contact at the edges of the cylindrical shell. The second approach is to measure the imperfections in the loading plate. Park et al. did not consider this approach since no measurements were performed on the loading plate.

1.1.3 Concluding Remarks

The discussed results show that imperfections affect the post-buckling behaviour of stiffened panels. The effect is mainly observed globally when the stiffeners carry the loads. Therefore, including imperfections is necessary for accurately analysing stiffened panels and their post-buckling behaviour. Modelling geometric imperfections has been well presented in the literature [12, 14], but not loading imperfections. Only the study conducted by Park et al. [26] has addressed the modelling of loading imperfections for composite stiffened panels. Further research is necessary to validate the load-displacement and offset trends observed in their work. Moreover, exploring the applicability of these trends to a different structural configuration also requires additional research.

1.2 Research Objective

Based on the literature review, it was understood that imperfections influence the post-buckling behaviour of composite-stiffened panels. Geometric imperfections are usually modelled using either measured imperfections, or, eigenmodes. In the case of the latter, the first few modes are often imposed from an eigenvalue analysis as an initial state for a non-linear analysis. This second method is used in the present study.

To the authors' knowledge, loading imperfections for straight stiffened composite panels are only included in the study from Park et al. [26]. However, they do not mention the influence of such imperfections on post-buckling behaviour. This presents a notable research gap, necessitating further investigations for more conclusive results. They are to be verified with the trends observed in the research from Park et al.

For the present thesis, the focus will be on a low-torsional panel with L-shaped stiffeners, due to their common use in aerospace applications. The thesis will also systematically analyse the inclusion of geometric imperfections in an FE paradigm. The previous literature has demonstrated the importance of including these imperfections in order to obtain more accurate models that allow for a better understanding of the observed post-buckling behaviour. Additionally, loading imperfections are modelled in this research to study how they affect post-buckling. Therefore, the main objective of this thesis can be summarised as:

To systematically show the influence of geometric and loading imperfections on the onset of buckling and post-buckling behaviour of an L-stiffened composite panel using finite elements.

To study the influence of imperfections on post-buckling behaviour, a baseline FE model was desired. For this, a stiffened panel design from Lanzi et al. [29–32] was modelled in ABAQUS, whose buckling behaviour is ought to be validated using their experimental data. A main research question and supporting questions are defined to meet this objective. The sub-questions (SQ) are presented with hypotheses (H), which are based on what has been learned from the literature until now.

Main research question:

What is the influence of geometric and loading imperfections on the post-buckling behaviour of L-stiffened composite panels?

Sub-questions and hypotheses:

SQ1 - Which buckling modes can be employed to more accurately represent the geometrical imperfections and observe responses according to experimental data?

H1 - The literature [19, 22] has presented strategies that include the use of eigenmodes from the linear eigenvalue analysis for geometric imperfections. Based on these studies, this thesis hypothesised that the first modes of the eigenvalue analysis will generate more representative results than higher modes close to the ultimate load.

SQ2 - How can loading imperfections be modelled effectively to align the responses of the FE model with experimental data?

H2 - In this thesis, it was hypothesised that loading imperfections through the tilted angle approach, as suggested by Park et al. [26] can accurately represent the experimental data.

SQ3 - How do geometrical and loading imperfections influence the onset of buckling and the post-buckling?

H3 - For geometric imperfections, it could be inferred from the literature [14, 24] that they have an influence on the ultimate load. Hence, in this thesis it was hypothesised that the geometric imperfections will only influence the ultimate load for the L-stiffened panel model. This is also hypothesised for the loading imperfections. In addition to this, based on the work of Park et al. [26], it is expected that a similar offset trend is going to be observed from the experimental data.

1.3 Thesis Outline

First, the FEM model that will serve as baseline is explained in detail in Chapter 2. Subsequently, Chapter 3 elucidates the methodology for modelling geometrical and loading imperfections in this baseline model. The influence of different imperfections were inferred from the study and also presented here. In Chapter 4, these observations are used to analyse and discuss post-buckling behaviour. Chapter 5 concludes the findings from this thesis, which helps answer the research questions and examine the hypotheses. The recommendations in Chapter 6 include a proposed experimental test methodology for assessing loading imperfections.

2

Baseline Model

As became evident from the previous chapter, the objective of this thesis is to systematically analyse the influence of imperfections on post-buckling behaviour for a composite L-stiffened panel. To do so, a baseline model is created with FEM due to its capability to simulate complex physical problems. The buckling behaviour of this model is then validated using data from Lanzi et al. [29–32]. In the following chapter, this validated model serves as a baseline for conducting additional studies.

First, Section 2.1 presents the reference case and explains the experimental conditions. This is followed by Section 2.2, detailing the construction of the baseline model, whose buckling behaviour is then validated in Section 2.3 using experimental data from Lanzi et al. [29–32].

2.1 Reference Case

The test approach of Lanzi et al., from now on referred to as *Lanzi case*, is straightforward: Axial displacement-controlled tests are performed on two pristine panels with a shortening velocity of 0.05 mm/s. The panels have L-shaped stiffeners and theoretically the same characteristics, but as later will become clear, there is a deviation in the experimental results. The material used is woven carbon fibre-reinforced plastic (CFRP), see Table 2.1, with $[0,90]_S$ layup for the stiffeners and $[45,0]_S$ for the skin. The zero-degree plies in the skin and stiffeners are aligned along the loading direction. The stiffeners and skin undergo separate manufacturing processes before joining through adhesive bonding and riveting. The testing setup is illustrated in Figure 2.1, and a schematic overview of the panel is shown in Figure 2.2. The panel is clamped using two longitudinal beams for the top and bottom surfaces. End tabs are used for the corners to constrain translational and rotational degrees of freedom (not visible in Figure 2.1) [29]. Based on the available data, it was unclear whether the dimensions provided for the panels included the clamping system, as further elaborated in Section 2.2.1. Regarding the measuring approach, the axial shortening in the setup is measured using two linear variable differential transformer (LVDT) transducers, placed close to the free edges. This is done to ensure that the measured shortening is not affected by deformations of the clamping system. The load history is measured with a load cell, referred to as MTS load cell in the figure.

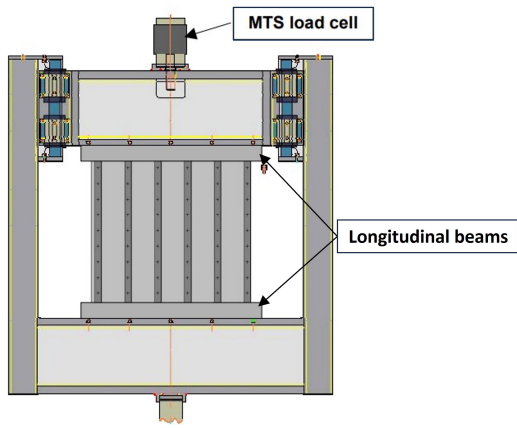


Figure 2.1: Schematic overview of the testing setup, copied from [29].

Table 2.1: Mechanical properties, adapted from [30].

Property	Value	Unit
Elastic modulus $E_{11}=E_{22}$	55700	[N/mm ²]
Shear modulus $G_{12}=G_{13}=G_{23}$	3060	[N/mm ²]
Poisson coefficient $\nu_{11}=\nu_{22}$	0.048	[-]
Tensile strength $\sigma_{11}=\sigma_{22}$	431	[N/mm ²]
Compression strength $\sigma_{11}=\sigma_{22}$	467	[N/mm ²]
Shear in-plane strength τ	99	[N/mm ²]
Ply thickness	0.33	[mm]

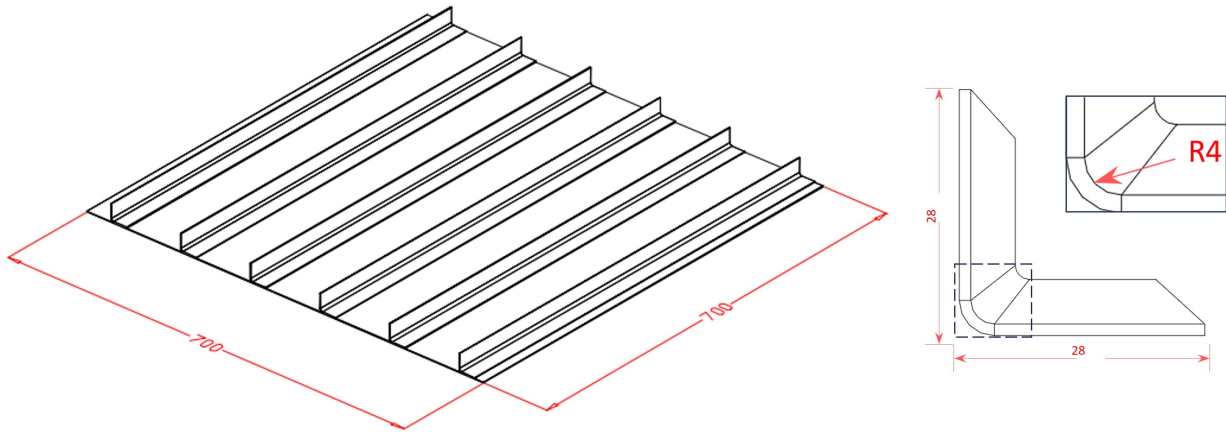


Figure 2.2: Stiffened panel dimensions in mm: Skin is shown on the left (Figure Courtesy: [29]), and L-stiffener on the right.

2.2 Finite Element Implementation

The FE models are created in the commercial software ABAQUS 2023. Two modelling approaches are followed to create a model with the closest characteristics to the Lanzi case. The first model employs conventional S4R¹ elements, and the second SC8R² continuum shell elements. The former requires less computational effort than the SC8R element-containing models. Both element types account for transverse shear deformation. However, their through-the-thickness behaviour differs: the S4R elements capture the properties in the mid-plane of the element and are formulated assuming plane stress, whereas the SC8R continuum shell model allows for stacking of the elements and features a constitutive relation for out-of-plane stresses. In the present study, SC8R elements are implemented by stacking four elements along the thickness direction, one for each ply. A mesh convergence study is performed to ensure that the final load-displacement curves are mesh-independent.

¹Quadrilateral conventional 4-node general purpose shell with reduced integration [33].

²Quadrilateral continuum shell element with 4-nodes facing the bottom-, and 4-nodes facing the top surface [33].

The axial compression load as well as the corresponding displacement (axial shortening) are important outputs for the studies performed on imperfections, as will become clear in Chapters 3 and 4. The study resulted in a mesh size of 5 mm x 5 mm for both the S4R and SC8R models, with their respective element types assigned, after refining the mesh until the loads converged. However, further mesh refinement was required around the stiffener fillet (Figure 2.3) to adequately cover the high-stress gradients in this region. The fillet region is depicted in an enlarged view within Figure 2.2. In Figure 2.3, the mesh for the stiffener is depicted, and as it becomes clear, 10 elements are used along the curvature of the stiffener fillet. Also, the number of elements along the width of the stiffener can be deduced: 5 elements along both sides. No further mesh study was needed through the thickness of the SC8R model as the four-element mesh already gave converged results. The complete mesh convergence study is presented in Section A.2.

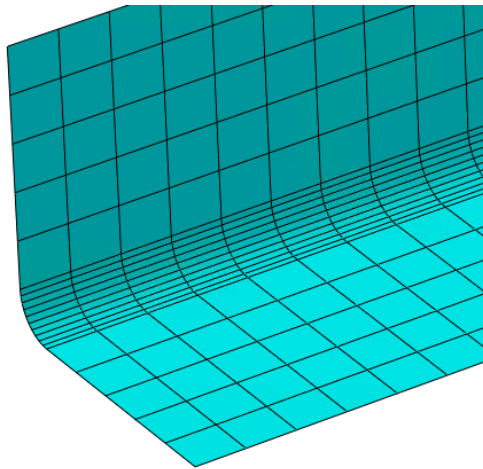


Figure 2.3: Detail view for the meshed stiffener with 10 elements along the fillet and 5 elements along the short edges.

2.2.1 Boundary Conditions

The boundary conditions are selected to replicate the experimental setup as accurately as possible. Referring back to the setup illustrated in Figure 2.1, the panel is clamped on both the top and bottom sides, except for the loading direction (U_2) at the top. In ABAQUS, this is modelled by tying the top and bottom edges of the skin and stiffeners to their respective reference points with the corresponding restricted degrees of freedom. This is depicted on the left in Figure 2.4 for the S4R model. The longitudinal edges are left free. While conventional shell models have displacement and rotational degrees of freedom, continuum shell models are restricted solely using the displacement degrees of freedom.

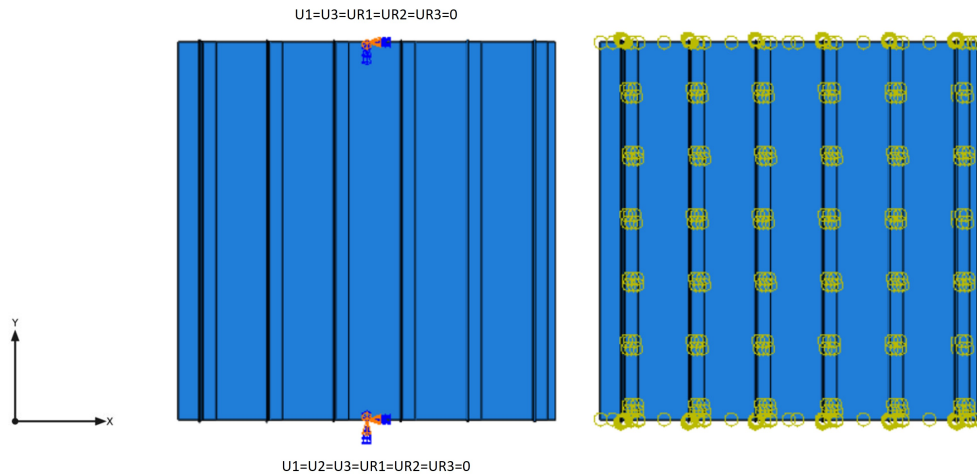


Figure 2.4: On the left, the applied boundary conditions are shown, and the right depicts the tie constraint of the skin and stiffeners.

The information about the clamping mechanism and clamped surface area could not be well-understood from the published work of Lanzi et al. [29–32]. It is crucial to accurately model the surface area, as this contributes to the creation of a validated model that closely represents the buckling behaviour of the Lanzi case. Hence, a trade study was conducted. In literature [25, 34], it is commonly observed that the ends of such stiffened panels are potted for a better introduction of the loads. The potting has the purpose of clamping the edges and preventing local buckling or compression failure at the ends [34].

In the FE models, the potting region was modelled in the form of boundary conditions to simulate the potential clamped region: in Figure 2.5, this region is illustrated in the left figure. The estimation of the potted surface area was approximately 50 mm from the edges, determined by counting the pixels in the images provided in the study by Lanzi et al. [29]. Within this region, both the out-of-plane (U_3) and the in-plane transverse displacement (U_1) are restricted. For additional details, refer to Section A.1. Nonetheless, this method was ultimately disregarded due to an observed error rate that was higher than in the Lanzi case, as detailed in Figure A.3. As an alternative, the complete surface area was included in the analysis, depicted on the right in Figure 2.5, which resulted in better agreement. For a more comprehensive explanation of the results obtained from the modelling iterations, including the potted model, before arriving at the final baseline model, refer to Appendix A.

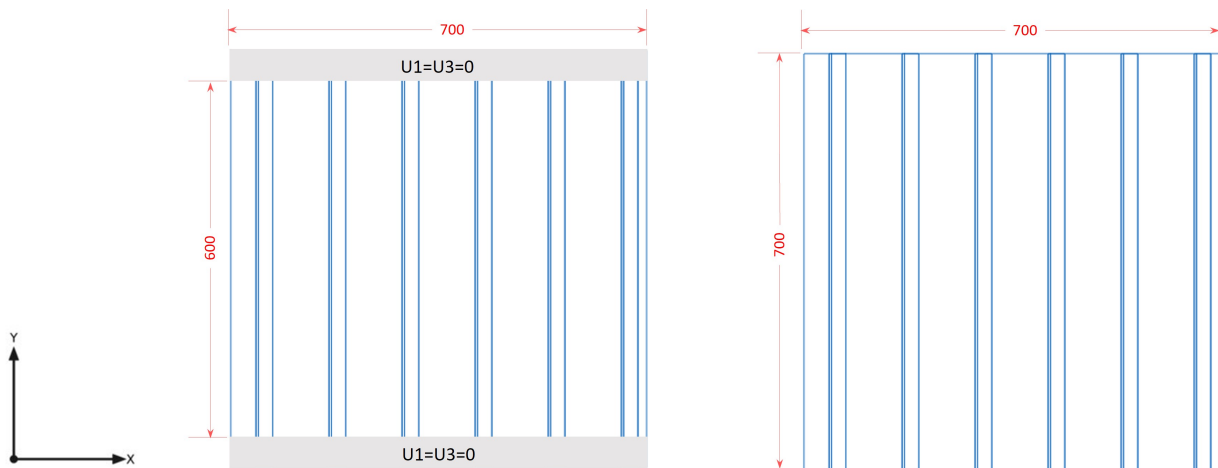


Figure 2.5: On the left, the grey regions are the potted area (not to scale), while on the right figure, no potting is included.

As mentioned earlier, the Lanzi case specifies that the skin and stiffeners undergo separate curing processes before bonding and riveting. In the FE model, the lack of available data on the adhesive used prevented modelling this region. As for the rivets, it is assumed that these joints are sufficiently rigid to act collectively as a single rigid body. This has been represented using a tie "surface-to-surface" constraint, allowing the stiffener flange to deform alongside the skin. In the model illustrated on the right side in Figure 2.4, this feature is depicted by yellow symbols, indicating the tied regions. Not previously mentioned, but to prevent mesh distortion caused by the tie constraint, the meshes for the skin-stiffener interface have been aligned, as shown in Figure 2.6, resulting in coinciding nodes.

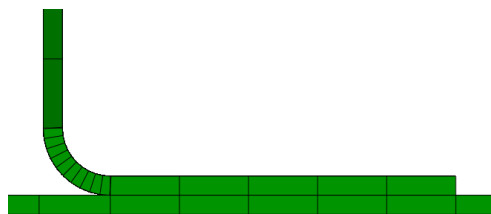


Figure 2.6: Visualisation of the aligned meshes.

2.2.2 Analysis Methods

An eigenvalue and a dynamic implicit (DI) analyses were performed for the FE models. The eigenvalue analysis is based on a linear pre-buckling state, and is used to determine the linear buckling load. In addition to this, the linear buckling eigenmodes are used to model geometric imperfections, as detailed in Section 3.1. The DI analysis has the benefit of considering inertia effects and improved convergence behaviour compared to general static analysis, especially during dynamic events such as the stiffness reduction at buckling and the later buckling mode changes.

A challenge imposed by DI analysis is the selection of the correct displacement velocity rate, as it can affect both the computational time and the convergence of the solution. At high

velocities coupled with sudden changes in the stiffness of the structure, the solution may diverge. ABAQUS's built-in automatic time incrementation algorithm attempts to mitigate this by reducing the time increment. However, even with a decreased time increment, the solver may still encounter overshooting issues followed by sudden load drops rather than normal convergence. Low velocities on the other hand, lead to increased computational costs. The shortening velocity by Lanzi et al. [29] is for this reason not adapted. Based on a convergence study that concentrated on the load-axial shortening relation, the analysis initially commenced with a velocity of 1.3 mm/s and subsequently decreased to a rate of 0.13 mm/s. Ultimately, this study led to the selection of a velocity of 0.13 mm/s for both the S4R and SC8R models. The findings of this study are presented in Section A.3.

2.3 Validation

The experimental data and the obtained results from the FE models are shown in Table 2.2. Starting with the outcomes of the two-panel tests conducted by Lanzi et al. [29], referred to as *Panel 1* and *Panel 2*, their initial stiffness is equal, even though there is a small difference in the first buckling load. The most notable observation is the difference in their ultimate loads, which is approximately 12%. According to Lanzi et al. this could have arisen from the differences in collapse modes: in the case of Panel 1, the failure was observed at half the height of the stiffener web (Figure 2.7) - assuming that the authors refer to the vertical section of the stiffeners, perpendicular to the skin. At these locations, the bending stresses were higher than in the rest of the panel. Panel 2 also fails at the stiffeners, but at the top and bottom parts. In both cases, Lanzi et al. state that the sudden failure of a stiffener redistributes the stresses, ultimately leading to the final structural collapse occurring at different loads.

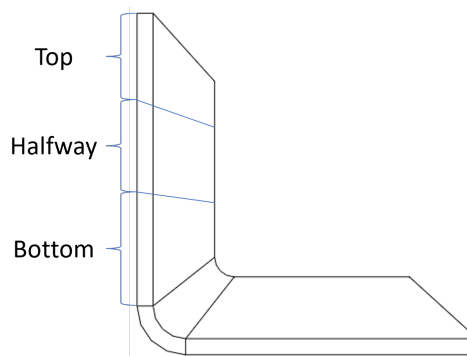


Figure 2.7: Illustration of the three regions in the stiffener web.

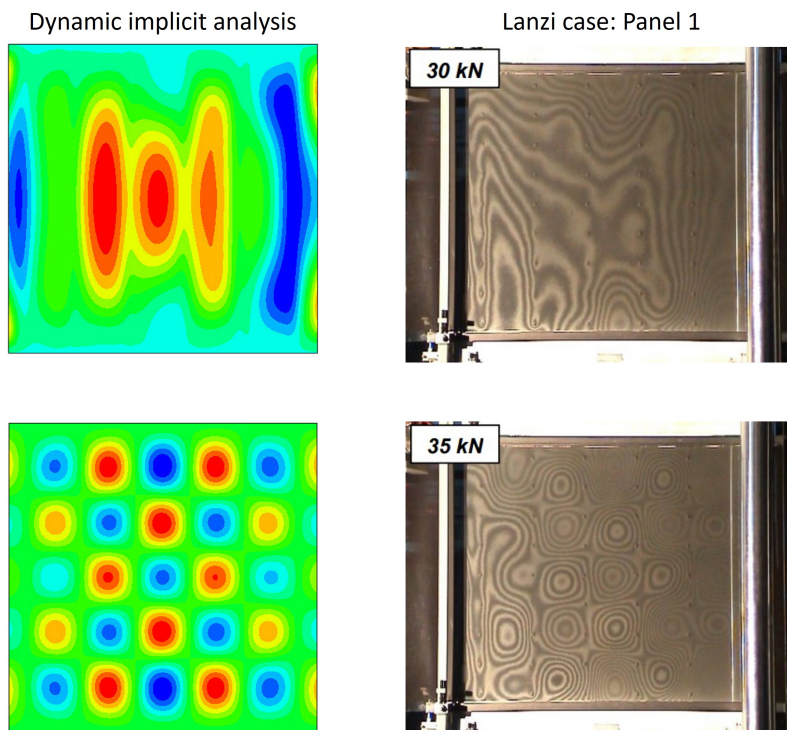
It is noteworthy that the authors did not consider additional factors like possible defects arising during the manufacturing of individual parts or defects introduced during the skin-stiffener joining process.

The final two columns of Table 2.2 show the FE model results. The models show remarkably similar outcomes. They also align closely with the characteristics of Panel 1.

Table 2.2: The experimental data from the Lanzi case [32] and results obtained from the FE models.

Description	Lanzi case		FE model	
	Panel 1	Panel 2	S4R model	SC8R model
First buckling load [kN]	32.9	29.8	34.3	34.6
Axial shortening at the first buckling load [mm]	0.39	0.36	0.39	0.40
Initial stiffness [kN/mm]	83.7	83.5	87.9	86.5
Ultimate load [kN]	66.7	75.4	67.5	67.8
Axial shortening at the ultimate load [mm]	1.17	1.37	1.02	1.02

Given that the S4R and SC8R models have demonstrated nearly identical results, for simplicity, only the S4R model is compared with Panel 1. The comparison is only made with respect to Panel 1 since the buckling mode shapes were only provided for this panel. Figure 2.8 illustrates the out-of-plane behaviour during linear buckling for both Panel 1 and the S4R model. The modes and corresponding loads are compared. The top two figures show the transition before reaching the first buckling load. The DI analysis displays a trend similar to that observed in Panel 1. The comparison between the first buckling mode from the DI analysis and the experimental data is presented in the second row. The results again demonstrate similarities in terms of the number of half-waves and exhibit similar buckling trends. In both the horizontal and vertical directions, five half-waves are observed in the FE model and the experimental data.

**Figure 2.8:** Comparison of linear buckling shape on the unstiffened side: FE S4R model (left) and experiment results of Panel 1 (right) [29].

In Figure 2.9, the loads are plotted against the shortening for the two FE models and Panel 1 and 2 from the experiment. To summarise, comparing the baseline FE models and the experimental data of Panel 1, two differences can be pointed out: stiffness varies after a shortening of approximately 0.4 mm (see Figure 2.9), and the axial shortening at ultimate loads varies by 13% (Panel 1- 1.17mm and; S4R model-1.02 mm). Refer back to Table 2.2 for the shortening values.

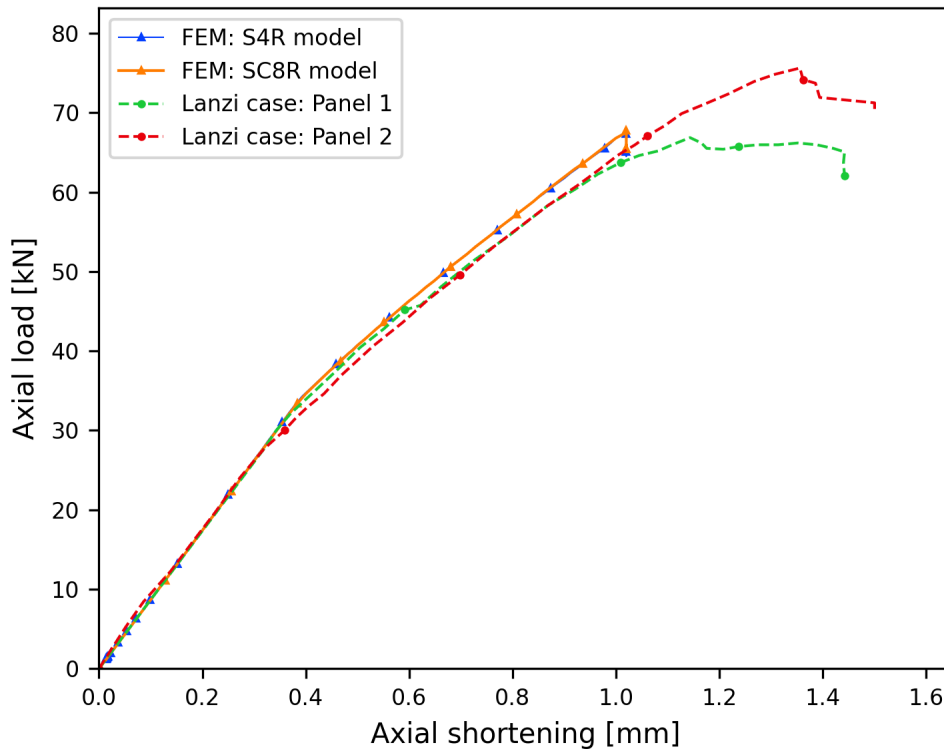


Figure 2.9: Experimental data [29] compared with FE models.

For the FE analysis, the simulation was terminated after a drastic load drop at around 67 kN for an axial shortening value of approximately 1 mm (Figure 2.9). After the load drop, the number of half-waves remained at five in the horizontal direction; however, in the vertical direction, it switched from five to seven half-waves. In real-life scenarios, such mode jumps may lead to a sequence of events, including delamination and cracks followed by crippling, or vice versa, as noted by Williamson et al. [35]. These phenomena result then in the degradation of the panel's properties. This claim can be further supported by the experimental work of Faggiani et al. [36], that showed an audible snap following the mode jump in their I-stiffened panel, accompanied by the sound of cracking. Moreover, Dávila et al. [37] also observed delamination followed by crippling in their tested stiffened panel, leading to ultimate failure.

Nevertheless, the FE model developed in the present study does not account for all possible failure modes. For example, interlaminar damage like delaminations and intralaminar damage, such as the formation of transverse cracks, are not modelled. To further solidify the rationale behind terminating the simulation subsequent to the load drop, it is hypothe-

sised that the failure occurred due to the crippling - local failure - of a stiffener. An accurate representation of this failure mode would require a progressive damage and failure model for fibre-reinforced composites, which is not implemented.

A hypothesis is formulated based on what was mentioned at the beginning of this section: Lanzi et al. [29] stating that the structural failure of both panels in the experiment is caused by the local failure of a stiffener. To effectively verify this, two failure modes are checked: the first involves checking for material failure, which could indicate damage such as delamination or crack formation prior to crippling. The second mode investigates whether stresses in the stiffeners exceed the critical, crippling stress, serving as an indicator of crippling failure.

The structure is first checked for material failure by performing a ply-level stress analysis. The Tsai-Hill criterion was used to check for first-ply failure [38]. The equation below shows the stresses that are read from the FE models: the tensile, compression and shear stresses. When the failure index F surpasses "1", it marks the occurrence of first ply failure.

$$F = \frac{\sigma_{11}^2}{\sigma_{11}^2} - \frac{\sigma_{11}\sigma_{22}}{\sigma_{11}^2} + \frac{\sigma_{22}^2}{\sigma_{22}^2} + \frac{\sigma_{12}^2}{\sigma_{12}^2} \quad (2.1)$$

The value did not surpass 1, so the criterion was not met. This could be attributed to the modelling approach used for the skin-stiffener connection, which assumes a perfectly bonded region. There is also the option of applying other material failure criteria, such as Hashin's [39] or Puck's failure criteria [40]. However, the required material data were not available.

The models were then reviewed for crippling using an empirical formula: the one-edge-free stiffener formula from Kassapoglou [41] (see Equation 2.2) was used. For the width (b) 26 mm (assuming no fillet but a straight 90-degree corner), thickness (t) 1.32 mm and as ultimate stress, the lower strength value of 431 MPa was selected as a conservative estimate (see Table 2.1). This resulted in a critical, crippling stress (σ_{crip}) of 109 MPa.

$$\frac{\sigma_{crip}}{\sigma_c^u} = \frac{2.151}{\left(\frac{b}{t}\right)^{0.717}} \quad (2.2)$$

In ABAQUS, the reading of the in-plane stresses is not straightforward. To compare the stress values, a critical section is selected, and the in-plane stress values for every ply through the thickness are taken and averaged. In Figure 2.10, the maximum value for a 0-degree ply is shown. Upon taking the average in this section, it resulted in approximately 115 MPa, exceeding the theoretical value of 109 MPa.

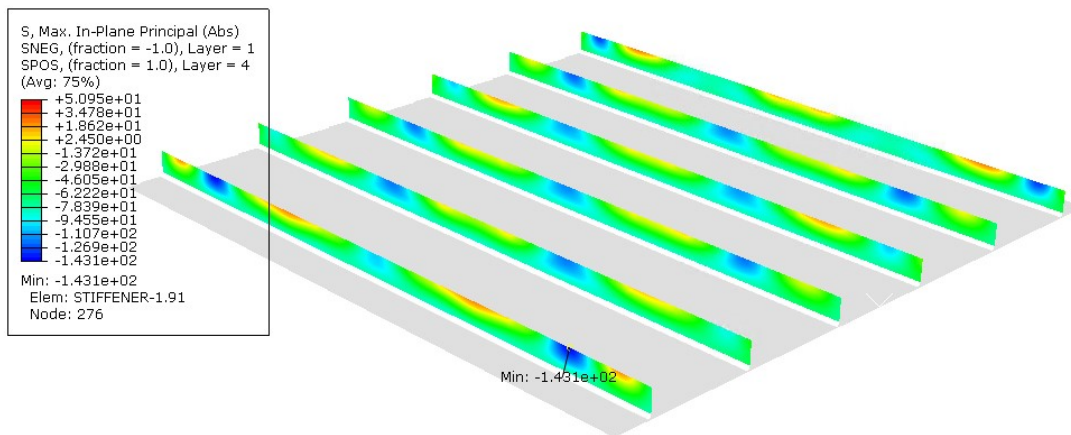


Figure 2.10: The maximum in-plane stresses encountered for a 0-degree ply at the point of load-drop.

The out-of-plane displacement corresponding to the stress distribution is notably high, as depicted in Figure 2.11.

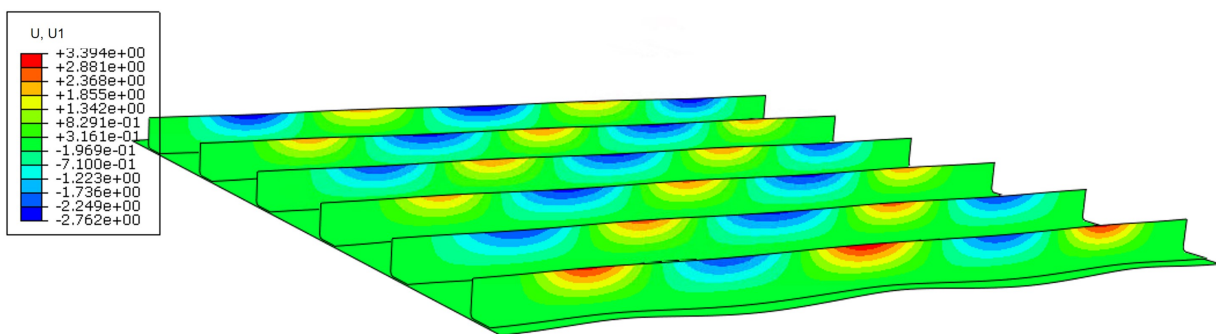


Figure 2.11: The out-of-plane displacements in the stiffeners at the point of load-drop.

In the FE model, while material failure thresholds were not exceeded, the surpassing of crippling stress suggests a potential for failure following the load drop. Literature indicates that such mode jumps may cause delaminations, consequently leading to crippling. Also, a tie constraint with coinciding nodes in the FE model can potentially result in a more conservative load distribution compared to what might be observed in the physical panels, as it overlooks factors such as joint behaviour, thus potentially underestimating the stress.

Another possibility is the (partial) debonding of the stiffener flange caused by rivets, leading to bearing failure. This reasoning is based on the bending of the stiffener flange (horizontal portion of the stiffener) and skin: see Figure 2.12 displaying a detail view on Figure 2.10. Additionally, critical stress levels are observed at the fillet region, indicated by the red area in Figure 2.12.

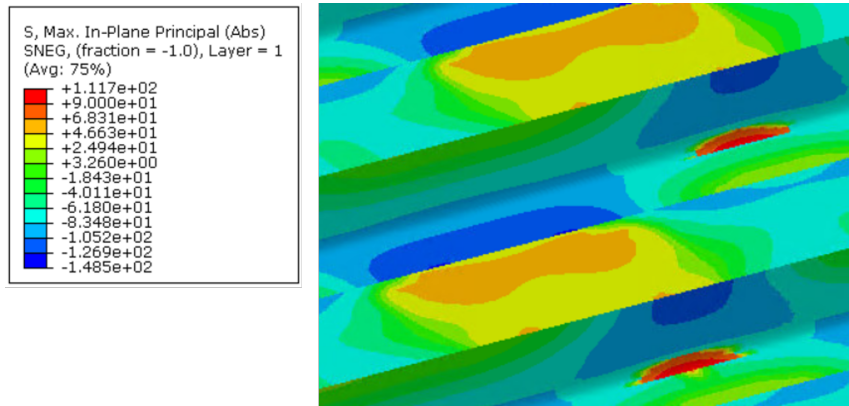


Figure 2.12: Detail picture of the stress region shown in Figure 2.10.

From Figure 2.13, it is notable that the skin exhibits out-of-plane displacement in the unstiffened direction. It is assumed that the stress behaviour shown in Figure 2.12 is influenced by this.

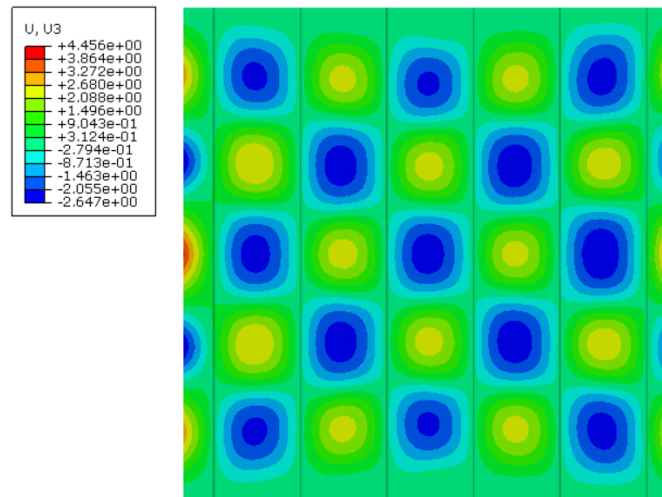


Figure 2.13: Out-of-plane displacement of the skin at the stress distribution shown in Figure 2.10.

Finally, the out-of-plane displacements for three different load cases are compared in the post-buckling regime with the Lanzi case in Figure 2.14. Lanzi case notes a range between -5 and 5 mm for the out-of-plane displacement [29], and the baseline model has a range between -2.6 and 4.5 mm. The negative values are displacements outwards, and the positive values are displacements inwards. While the maximum value (5 mm) shows good agreement, the minimum value (-5 mm) deviates with a clear difference. Furthermore, the FE models effectively replicate post-buckling behaviour until five half-waves.

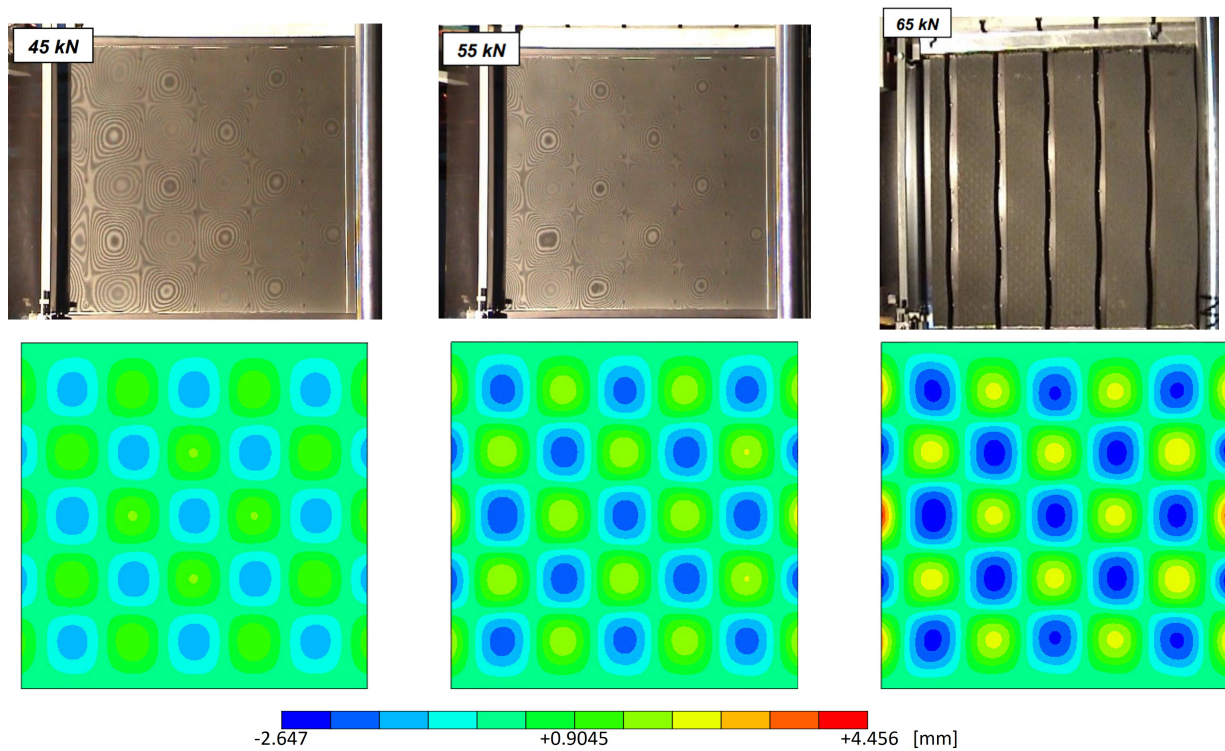


Figure 2.14: Out-of-plane displacements on the unstiffened side: Experimental data for Panel 1 (top) [29] and FEM S4R model (bottom).

To summarise, the FE models show a good agreement with the Lanzi case. The sudden load drop, leading to a mode jump, signals the necessity to terminate the simulation beyond this point, given that the failure modes occurring after this point are not modelled. This decision finds further support in the literature, which highlights that such sudden jumps can induce damage, including delamination. Although the material failure criteria were not exceeded, the observed high crippling stresses within the stiffener web, coupled with significant stress differences in the flange and skin, reinforce the rationale. Given that the FE model does not consider damage, their results are considered to be validated till the first load drop, beyond which the analysis is terminated.

The baseline FE models are now considered validated up to the load drop. These validated models serve as the foundation for the subsequent chapter, where additional studies are conducted to analyse the influence of geometric and loading imperfections on post-buckling behaviour.

Imperfection Modelling

The previous chapter established the validated baseline model for a stiffened panel case study. This chapter outlines the methodology followed for modelling imperfections, which is illustrated in the flowchart in Figure 3.1. In Section 3.1, the discussion covers the modelling of geometric imperfections and their influence on the baseline model. Likewise, the modelling and observed influence of loading imperfections are explained in Section 3.2. The final block in Figure 3.1 outlines the defined outputs used to identify the influence of these imperfections.

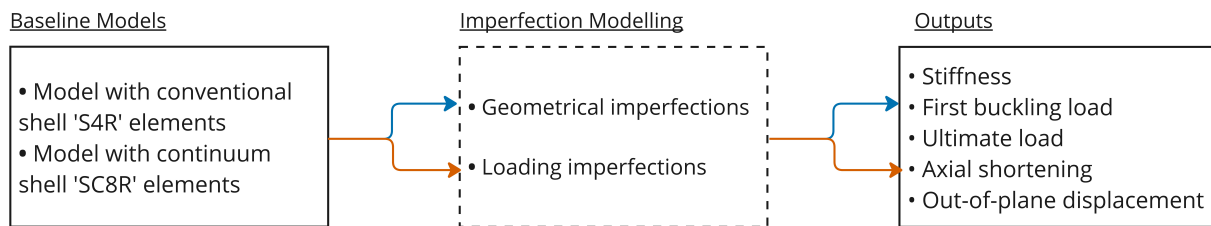


Figure 3.1: The steps followed to include imperfections in the models.

3.1 Geometric Imperfection

Various methods for modelling geometric imperfections exist, with some outlined in Chapter 1. One approach involves incorporating measured data directly from experimental observations. Alternatively, eigenmodes derived from a linear eigenvalue analysis can be employed. The first approach is not feasible due to the insufficient data available from the Lanzi case regarding the measurements of geometric imperfections. The second option, which assumes a shape based on linear buckling modes and modifies the respective nodes accordingly in FEM, is preferred. In this method, eigenmodes derived from a linear buckling analysis are used as the initial geometric state for DI analysis. These can be implemented as either a single mode or as a linear combination of multiple modes. This approach for the geometric imperfection w_0 is mathematically represented by the following equation:

$$w_0(x, y, z) = \sum_{i=1}^p c_i w_i(x, y, z) \quad (3.1)$$

where c_i are arbitrary scalar weighting factors applied to each linear buckling mode $w_i(x, y, z)$.

3.1.1 Modelling

The modelling strategies proposed by Schafer and Pekoz [20] and Gardner [21] are adapted as a modelling approach: combining at least two early linear buckling modes with different shapes. Choosing different mode shapes are crucial to prevent mode cancellation, which can occur when two modes with inverse deformations are superimposed. The weighting factor c_i , as shown in Equation 3.1, will be referred to as the amplitude from this point onward. These amplitudes are expressed as percentages of the skin thickness, which is 1.32 mm. The study by Lynch et al. [14] specifies 10% of skin thickness as a typical value for riveted structures. The present research involves testing a range of amplitudes from 1% to 10% to observe their influence on the stiffened panel.

As detailed in the upcoming section, a curve-fitting approach reveals that imperfection amplitudes up to 5%, yield results closely aligning with the initial baseline model. While real-life structures typically exhibit deformations equivalent to higher amplitudes, as also noted by Lynch et al. [14], it is important to clarify that these geometric imperfections do not manifest in mode-shaped deformations. This study imposes the buckling modes on the initial geometry to represent the geometric imperfections observed in experimental data. The modes are rather a tool to represent them within the FE paradigm.

In Figure 3.2, the first five eigenmodes for the baseline model are presented. The S4R and SC8R models showed identical modes, but for convenience, eigenmodes only obtained from the former model are depicted.

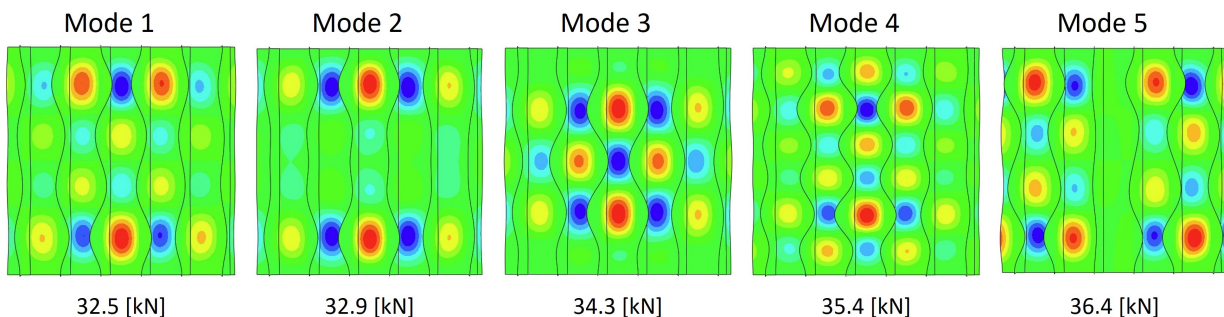


Figure 3.2: The first five eigenmodes of the baseline model.

Here, it is evident that modes 1 and 2 closely resemble each other as the half-waves appear at the same locations. One mode might be dominantly present in the physical realm, or a transition between the modes could occur. However, only the first mode was considered while making combinations, as these modes exhibit deformations in opposite directions. As previously noted, this opposing nature could lead to the cancellation of the modes when superimposed. All the considered mode combinations are marked with an 'x' in the following table.

Table 3.1: The combination of modes considered for the geometrical imperfections (marked with an 'x').

2nd mode \ 1st mode	1	2	3	4	5
1	-		x	x	x
2		-			
3	x		-	x	x
4	x		x	-	x
5	x		x	x	-

For the combination of modes 1 and 3, the former predominantly features half-waves at the edges, whereas the latter exhibits these more centrally on the panel. In the pairing of modes 1 and 4, mode 4 displays a concentration of half-waves in the centre, though some are present at the edges: these are minimal and unlikely to result in mode cancellation. With modes 1 and 5, potential cancellation effects may arise at the edges, yet the distinct behaviours of the skin in the midsection and edges for both modes mitigate this risk. Similarly, modes 3 and 4 show similarities, but additional waves are visible in mode 4, resulting in a unique half-wave distribution. As for combined modes 3 and 5, they exhibit unique half-wave patterns. Lastly, for modes 4 and 5, while the former is characterised by more pronounced half-waves in the midsection, the latter has half-waves distributed across the panel, excluding the centre.

The initial state of the model with the mode combinations were not able to be visualised due to the limitation of the solver used. However, their impact on the buckling mode shape of the baseline model is visually presented in Section 4.2.

3.1.2 Observations

The hypothesis presented for the research questions (in Section 1.2) suggested that using the first modes from the linear eigenvalue analysis to represent geometric imperfections would provide more accurate results compared to eigenmodes with corresponding loads close to the ultimate load (referred to as higher modes). Additionally, it was observed that these imperfections would primarily influence the ultimate load. The figures in this section depict varying amplitude ranges for load-displacement curves, illustrating differences between the first and higher mode combinations. The data was manually extracted from ABAQUS and plotted.

This section focuses on the influence of selected mode combinations on the ultimate load and axial shortening values of the models. The objective is to identify combinations that yield plausible results. In this context, "plausible" refers to combinations that do not result in unrealistically high ultimate loads and sudden stiffness differences. And, similar to Chapter 2, the simulations are terminated after a load drop, because the outputs beyond this point are not representative of reality since failure is not accounted as mentioned earlier. The findings from this section will be discussed in more detail in Section 4.2, where the (post-) buckling behaviour is addressed.

The observations are presented and analysed by grouping graphs that exhibit similar behaviours. As mentioned earlier, amplitudes only up to 5% of skin thickness are presented for the S4R models. For completeness, the 10% amplitude plots can be referred from Appendix B.

Modes 1-4 and Modes 4-5

Starting with Figure 3.3, the model with an amplitude of 5% exhibits stiffness degradation compared to the other amplitudes. Such behaviour can result from the generation of bending moments, which increases the out-of-plane deformations. This rationale can be backed up by the work of Mercier et al. [42]. The load only stabilises after an axial shortening of approximately 1.3 mm, a behaviour that could be attributed to stress redistribution caused by the inclusion of imperfections. Similar behaviour is evident in Figure 3.4 at a 2% amplitude rate.

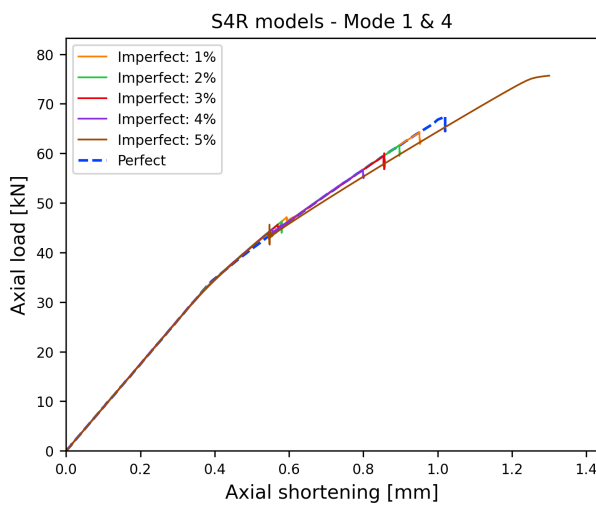


Figure 3.3: S4R models for Mode 1 & 4.

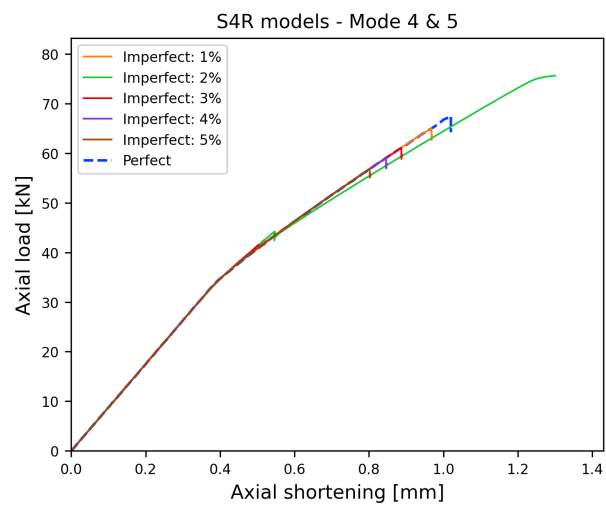


Figure 3.4: S4R models for Mode 4 & 5.

In both graphs, minor mode jumps are noticeable, such as in the line representing 2% amplitude in Figure 3.3. These jumps occur sufficiently early in the analysis, and it is assumed that they are small enough not to cause any damage, in contrast to the significant drop observed at the ultimate load. For further clarity, this jump is depicted in the following figure, where a distinct transition from four to five half-waves can be observed in the vertical direction of the panel.

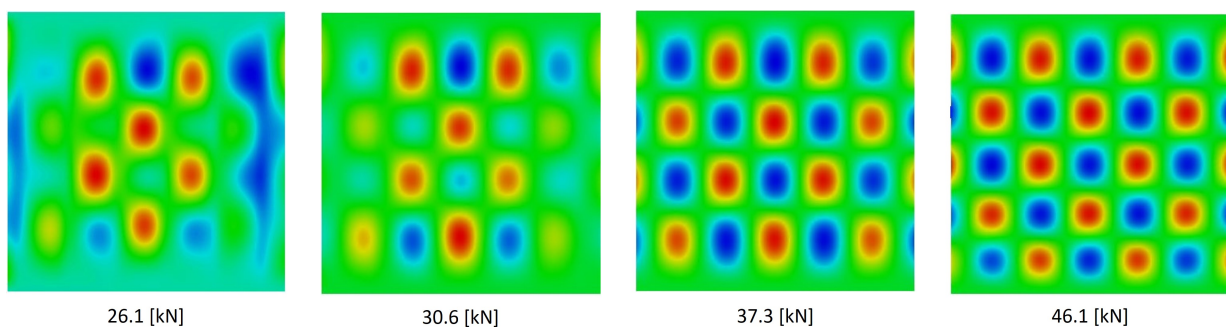


Figure 3.5: Mode jump for Mode 1 & 4 - 2% amplitude.

To provide further insight into the observed jump: Initially, as mentioned while discussing linear buckling modes in Figure 3.2, modes 1 and 2 exhibited very similar behaviours, suggesting the possibility of one dominating or a transition occurring in the physical realm. The jump noted in Figure 3.3 corresponds to the same load levels as eigenmodes 1 and 2, indicating that the inclusion of these imperfections with certain amplitudes triggered the potential mode interactions. Moreover, as suggested by Bushnell et al. [43], such interactions may indeed lead to jumps in structural response. Another possibility is that the mode jump is triggered purely by the imperfection shape and amplitude, independent of modes 1 and 2.

Moving on, the jumps can manifest at varying load levels, as seen in Figure 3.3: an imperfection with a 1% amplitude exhibits a jump at a higher load level. Observations indicate that larger imperfection amplitudes lead to lower buckling loads alongside a less intuitive buckling mechanism, where lower amplitudes might lead to lower ultimate loads because of a mode jump. This could be the case in Figure 3.4 for an amplitude of 2%. Drawing further from the study by Bushnell et al. [43], it is assumed that those jumps may not have enough energy content to damage the panel and impact its structural integrity.

Finally, the buckling behaviour for the remaining imperfection amplitudes shows expected trends, where higher amplitudes result in lower ultimate loads.

Modes 1-3 and Modes 3-5

When examining Figure 3.6, similar observations to those in Figure 3.4 (with a 2% amplitude) are made. It is noted that the ultimate loads for amplitudes of 3-4% are higher than those for a 2% amplitude, demonstrating a trend consistent with the counter-intuitive results observed in some of the previously discussed mode combinations. In contrast, the 5% amplitude exhibits the expected trend of a lower ultimate load compared to the other amplitudes.

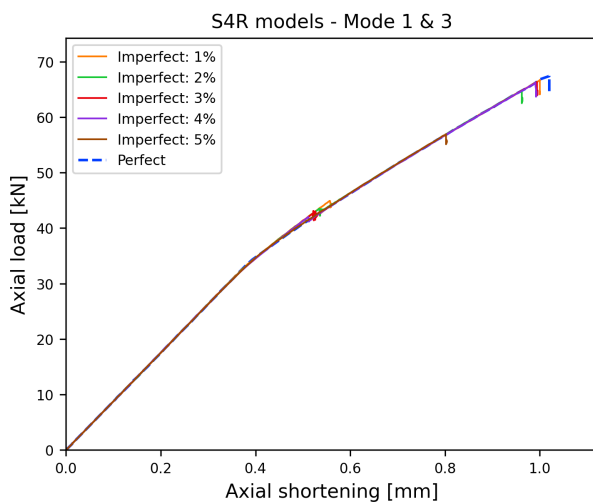


Figure 3.6: S4R models for Mode 1 & 3.

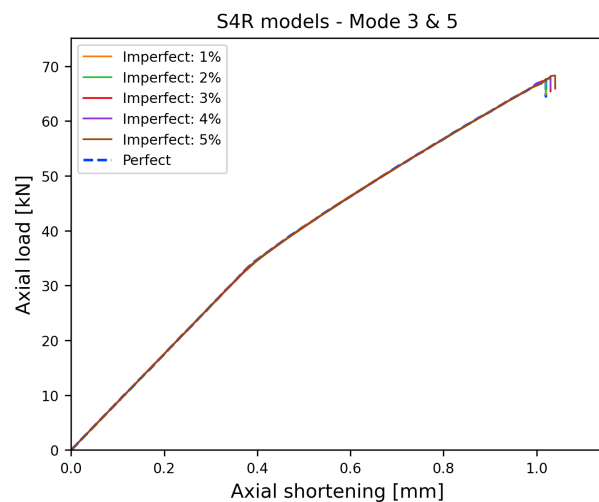


Figure 3.7: S4R models for Mode 3 & 5.

From Figure 3.7, it becomes apparent that this graph remains unaffected by increases in amplitude for the combination of modes 3 & 5. In fact, the ultimate load increases with the rising amplitude. Additionally, it does not exhibit any mode jumps, which is in contrast to the model with modes 1 & 3. This difference in behaviour can be attributed to the specific shapes

and amplitudes of the imperfections chosen for each model, as previously mentioned.

Modes 1-5 and Modes 3-4

Finally, figures 3.8 and 3.9 demonstrate a decrease in ultimate loads as the amplitudes increase. Both graphs show mode jumps, which could be attributed to a mode transition. As mentioned before, it is assumed that the structure can accommodate the load drop as it is relatively small and considerably distant from the ultimate load.

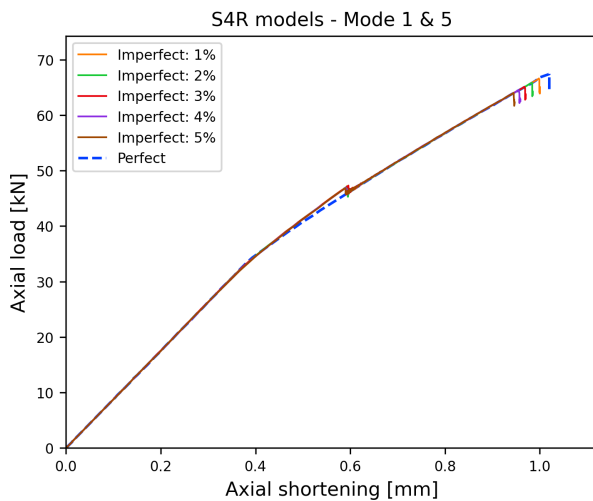


Figure 3.8: S4R models for Mode 1 & 5.

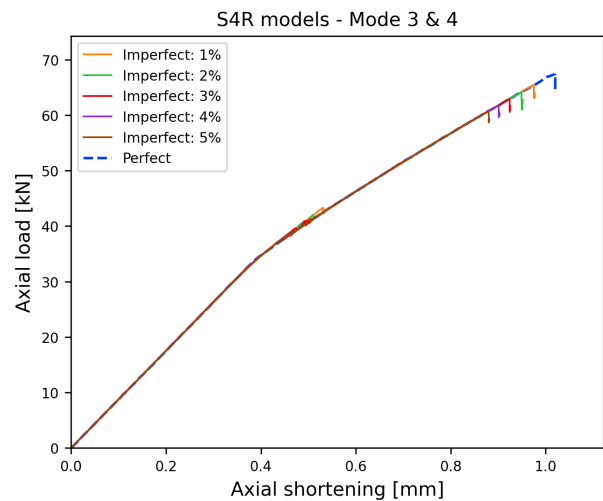


Figure 3.9: S4R models for Mode 3 & 4.

Summarising, the plots demonstrate expected behaviour in the first eigenmode combinations 1 & 5 and 3 & 4, with the former displaying ultimate loads closer to the perfect model and the latter showing consistent stiffness.

Higher Modes

The hypothesis for sub-question 1 (Section 1.2) suggested that the first eigenmode combinations would yield better results to represent geometric imperfections. To test this, eigenmodes are selected from the eigenvalue analysis with corresponding loads closer to the ultimate load. The selection is done by combining two modes with different half-wave shapes, as described earlier for the first modes. The following figure illustrates the selected modes.

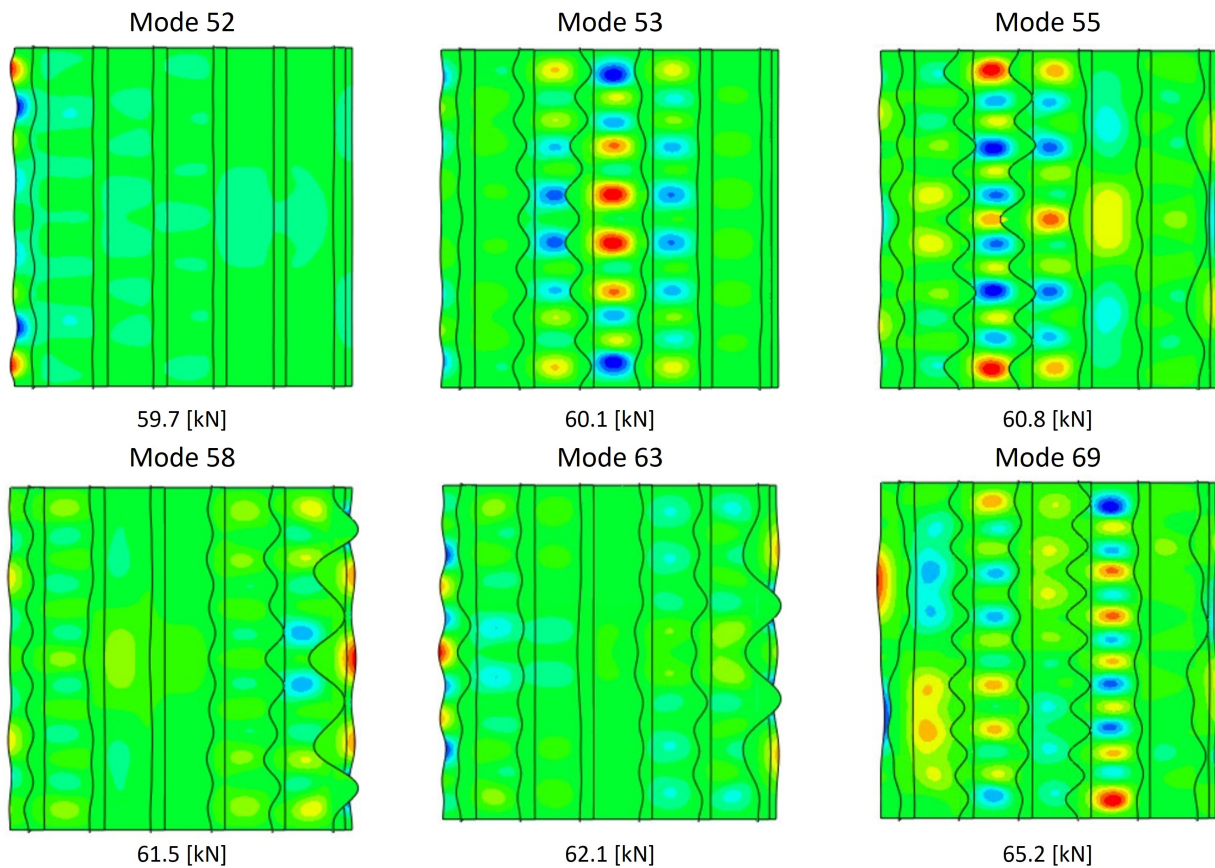


Figure 3.10: Eigenmodes near the ultimate load.

The combinations made are 52 & 53, 55 & 58 and 63 & 69. They all have unique half-wave patterns, and would not result in mode cancellation.

For simplicity, only an amplitude of 1% was implemented. The results revealed increased and decreased ultimate load, as visible in Figure 3.11.

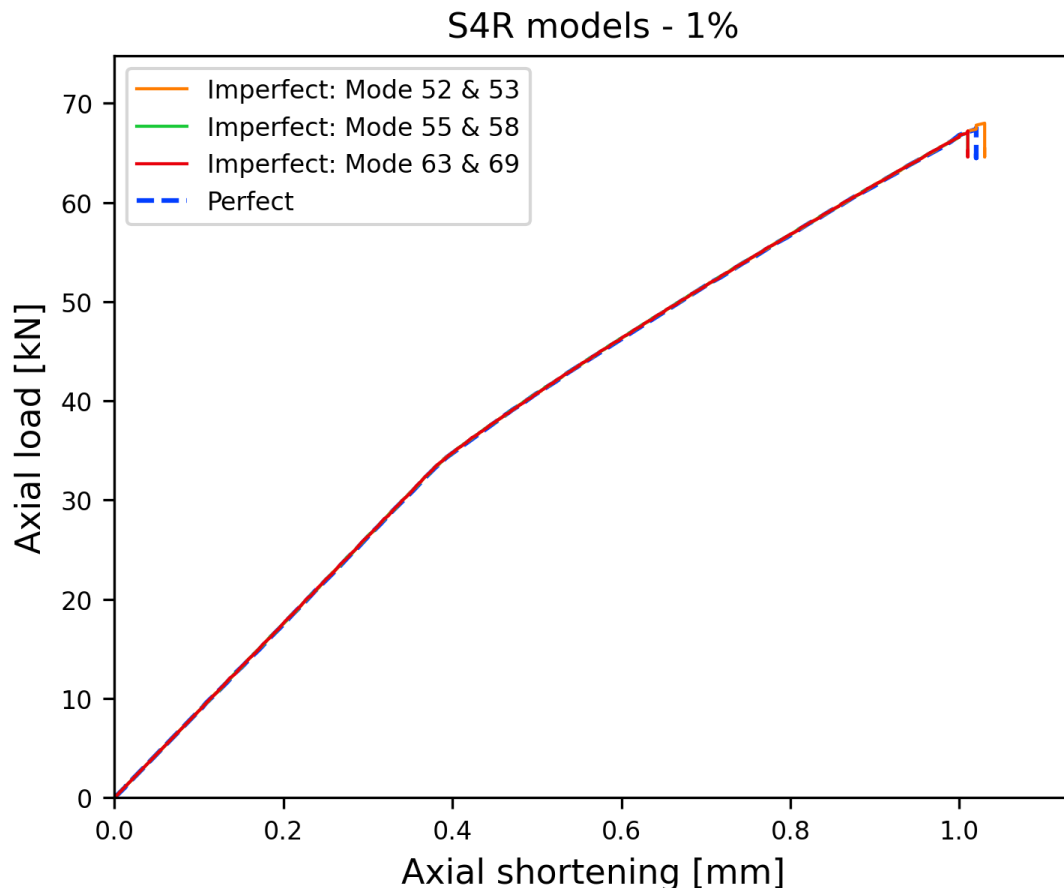


Figure 3.11: S4R modes with three different mode combinations.

It becomes evident that mode combinations 55 & 58, as well as 63 & 69, exhibit similar behaviour with ultimate loads lower than the baseline model. However, mode combinations 52 & 53 indicate a higher ultimate load. Besides this, there are no mode jumps or stiffness degradations visible, which was the case for the discussed results for the first mode implementation.

These findings indicate that, with careful selection, higher modes can effectively represent geometric imperfections. It becomes evident that the imperfection shape in the model does not need to mirror the post-buckled shape to accurately replicate experimental results. Rather, the selected imperfection combination should approximate the actual geometric imperfections of the tested panels, which are typically not known in advance. Accurately simulating these imperfections is crucial for triggering the same buckling mechanism observed in physical experiments. This approach ensures that the final post-buckled shape closely resembles the Lanzi case, thereby enhancing the model's reliability and predictive accuracy.

Moving on, the SC8R models showed similar behaviour to the S4R models. This can be seen in Figure 3.12, where the results of an amplitude of 1% for the combinations 1 & 5 and 3 & 4 are presented for both types of models. These trends show that both types of models without imperfection, or with the same imperfection, exhibit the same behaviour.

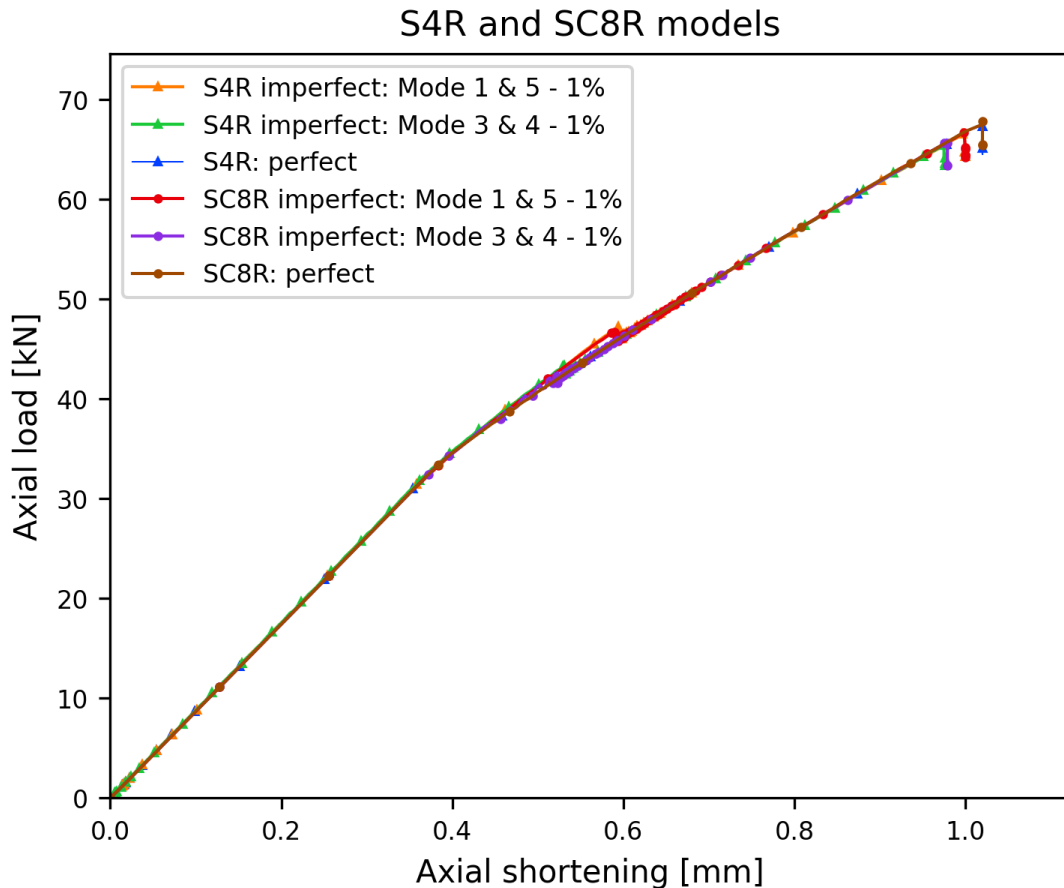


Figure 3.12: The relation between the S4R and SC8R models.

Based on Figure 3.12, only the S4R model appears adequate for modelling geometric imperfections. In the following chapter, the amplitudes 1 and 5% will be further discussed for the mode combinations 1 & 5 and 3 & 4 as they were found to model the geometric imperfections well.

3.2 Loading Imperfection

Adjustments are made to the baseline model to account for the impact of the loading imperfection. A loading plate is introduced as a discrete rigid body to transfer the loads to the stiffened panel. Previously, the loads were uniformly applied through reference points, tied to the edge of the panel. The addition of the loading plate was omitted due to the inclusion of a contact formulation, which imposes some stiffness between the stiffened panel and the loading plate. This adjustment is only made for the SC8R model. In the case of the S4R model, contact was not possible because of the element type that could not establish contact on the edge with the loading plate.

The stiffnesses seem equal in the plot shown on the left in Figure 3.13, where the baseline model is compared with the model including a loading plate. Upon a closer look - see the figure on the right - a small offset is visible after an axial shortening displacement of around 0.2 mm. The final axial shortening differs very clearly. This could be caused by the contact

formulation that includes a default value for an artificial contact stiffness, which introduces additional compliance to the model. This decreases, in this case, the overall stiffness.

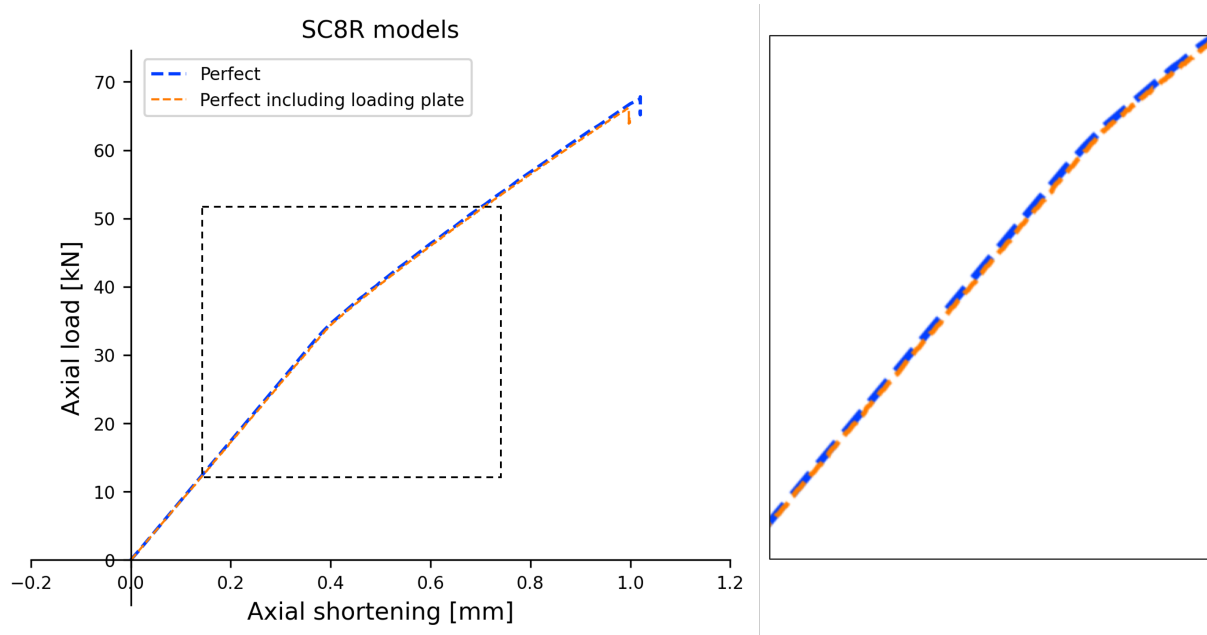


Figure 3.13: SC8R models for a perfect plate with and without loading plate (left) and a close-up of the graph (right).

3.2.1 Modelling

Recalling the work of Park et al. [26], they placed the loading plate at a tilted angle of 0.005 and 0.01 degrees with respect to their stiffened panel. This was done to resemble a less ideal loading scenario at the start of the experiment. A similar approach is taken in the present study and the loading imperfections are modelled using SC8R models in order to compare their (post-)buckling behaviour with the baseline model in Section 4.3.

As an initial step, four different configurations are tested in two setups, illustrated in Figure 3.14. The first configuration displays the front view, labelled as *Left* and *Right*, denoting the loading plate's orientation: in this instance, the panel is inclined towards the right side. The second figure portrays the side view, similarly marked to indicate the orientation.

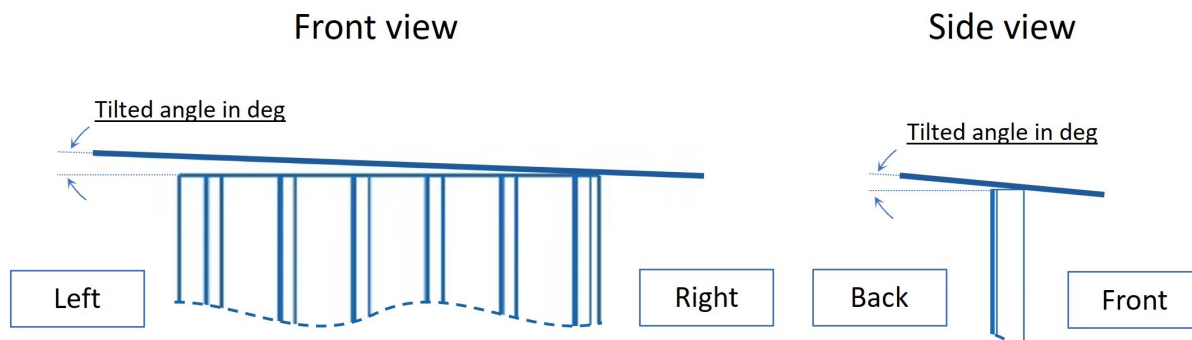


Figure 3.14: Overview of the configurations, with front view (*Left* and *Right* configurations) and side view (*Back* and *Front* configurations).

3.2.2 Observations

In figures 3.15 and 3.16, the analysis begins with a negative value, indicating that only a section of the panel is initially in contact with the loading plate. In the FE models, the displacement is measured at halfway of the loading plate. This negative axial shortening is represented by $\Delta_c = b \tan(\theta/2) \approx b(\theta/2)$ for small angle approximations. For instance, with a tilt angle of $\theta = 0.01$ degrees, this equation yields $\Delta_c = 0.061$ mm, quantifying the initial deviation before the full application of the load.

A higher tilt angle results in an increased offset and reduced ultimate load, as visible in figures 3.15 and 3.16. This trend is consistent for rotating the loading plate across both sides of the panel. The loading plate inclining more to the right edge, does result in a higher ultimate load compared to the left edge, possibly attributed to the closer proximity of the stiffener flange to the edge.

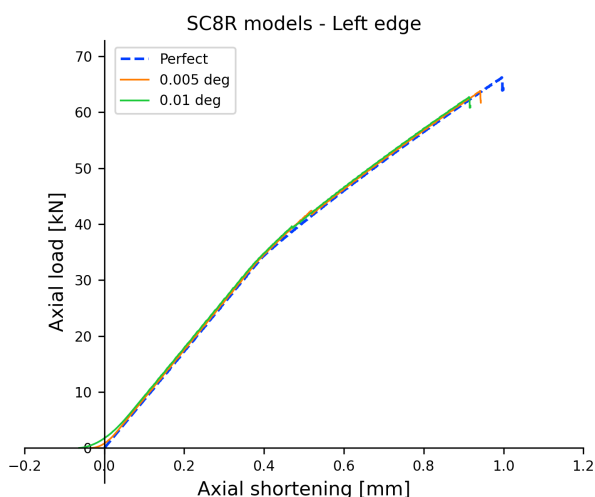


Figure 3.15: SC8R models: Loading plate tilted to the left.

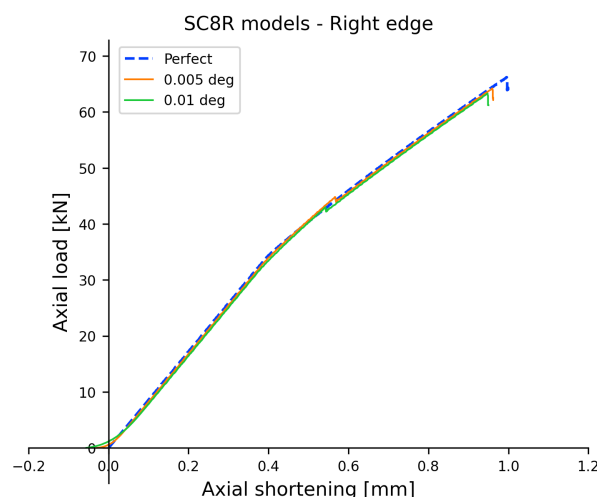


Figure 3.16: SC8R models: Loading plate tilted to the right.

From Figures 3.17 and 3.18 it can be inferred that inclining the loading plate along the back and front edges has minimal impact. The load drops around 0.6 mm are similar to what was

observed for models with geometric imperfections, and likely negligible.

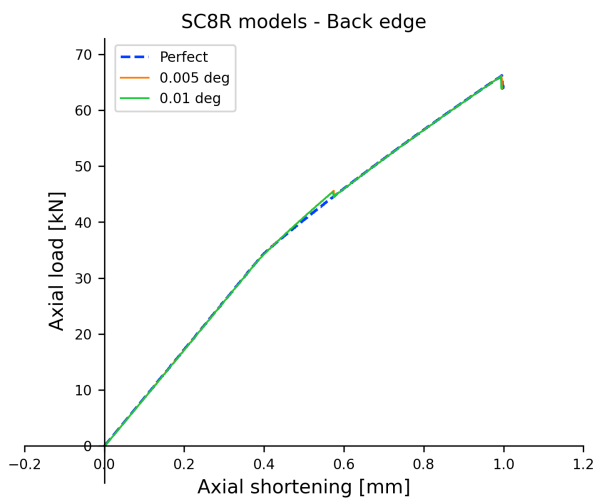


Figure 3.17: SC8R models: Loading plate tilted to the back.

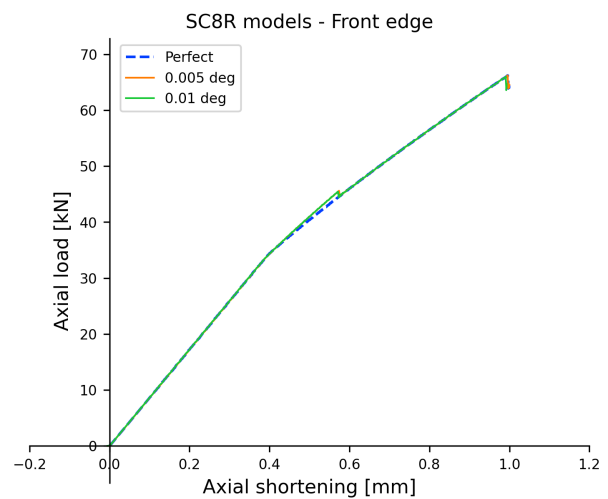


Figure 3.18: SC8R models: Loading plate tilted to the front.

3.3 Remarks

The observations in this chapter showed how modelling parameters of geometric and loading imperfections influence the behaviour of the panels. Geometric imperfections were found to be modelled well using Mode 1 & 5 and Mode 3 & 4 combinations with amplitude 1-5 %. For models including loading imperfections, the Left- and Right edge configurations resulted in more impact than the Back- and Front edge configurations. These modified models are used to analyse post-buckling behaviour in Chapter 4 based on the defined parameters at the start of this chapter.

4

Results and Discussion

The previous chapters established the baseline model and the inclusion of geometric and loading imperfections. In this chapter, the results obtained from these models will be further discussed based on the outputs defined in Figure 3.1: the initial stiffness, first buckling- and ultimate loads, the axial shortening, and the out-of-plane displacement. First, the differences between the obtained results for the tested panels by Lanzi et al. [29] are presented in Section 4.1. This is followed by the results for the geometric and loading imperfections, presented in Sections 4.2 and 4.3, respectively. While the baseline models are validated, the models with geometric and loading imperfections are still compared with experimental data by Lanzi et al. to understand the practical differences between the modified models and experimental data. This approach aims to show the observed correlations beyond what the validated baseline model revealed. Following these sections, a discussion is presented where the results are examined and interpreted in the context of the study's objective.

4.1 Results Lanzi case

Before discussing the results obtained from the models with imperfections, it is important to highlight differences between the two panels tested by Lanzi et al. [29], and recall the main sources of uncertainty. In Figure 4.1, a clear difference between the tested panels, especially in their ultimate loads, is visible. See Table 4.1 for the complete comparison with their respective deviations in percentages.

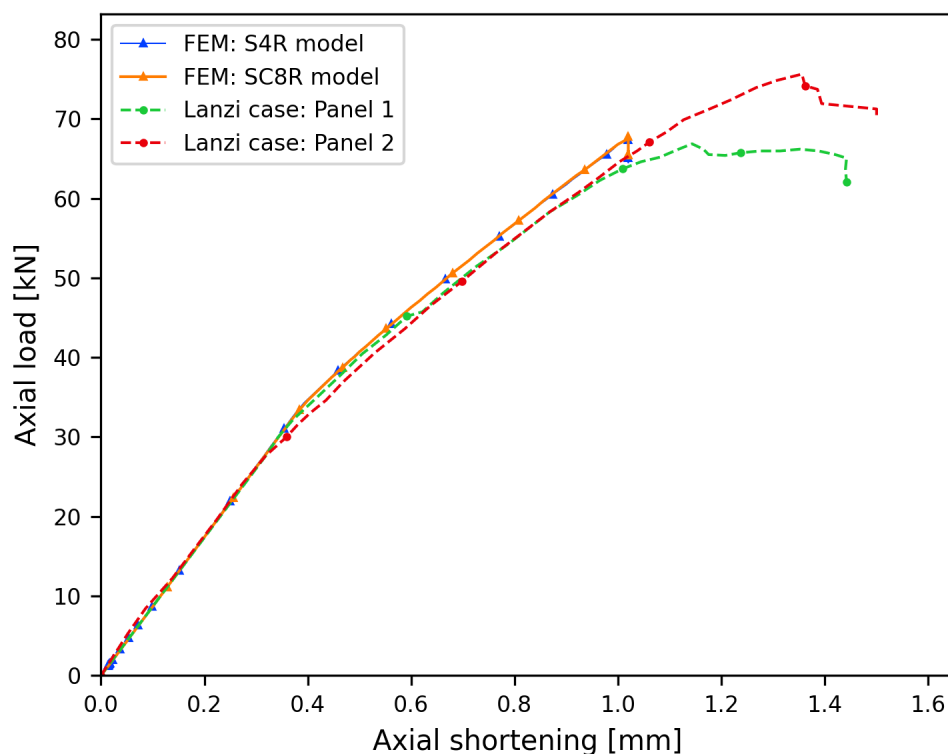


Figure 4.1: Experimental data [29] compared with FE models.

Table 4.1: The experimental data from the Lanzi case [32] and the percentage deviation between the panels.

Description	Panel 1	Panel 2	Deviation (%)
First buckling load [kN]	32.9	29.8	9.9
Axial shortening at the first buckling load [mm]	0.39	0.36	8.0
Initial stiffness [kN/mm]	83.7	83.5	0.2
Ultimate load [kN]	66.7	75.4	12.2
Axial shortening at the ultimate load [mm]	1.17	1.37	15.8

In Chapter 2, it was noted that Lanzi et al. attributed the discrepancy in their test results to the differences in the collapse mechanisms of their panels: Panel 1 failed at the stiffener web's half-height, while Panel 2 failed at the stiffener web's top and bottom sections. They emphasised that these variations highlight the sensitivity of post-buckling behaviour to different failure modes. Although the authors do not explicitly mention it, this study also assumes that these differences could, for example, be caused by manufacturing defects.

Regarding the comparison between the Finite Element (FE) model and the experimental cases, it is noteworthy to recall the differences between the tested panels. The FE model exhibits a lower percentage deviation for the different properties listed in Table 4.2 compared to the panels, especially with respect to Panel 1. Considering the deviation between Panel 1 and 2, which share the same material and design but still result in a notable difference, the presented FE model is already within an acceptable prediction range.

Table 4.2: Comparison of Panel 1 and 2 from experimental data with perfect S4R model and their deviation (%).

Description	Baseline model	Deviation (%)	
		Panel 1	Panel 2
First buckling load [kN]	34.3	4.2	13.1
Axial shortening at the first buckling load [mm]	0.39	0.0	7.7
Initial stiffness [kN/mm]	87.9	4.9	5.0
Ultimate load [kN]	67.0	0.5	12.5
Axial shortening at the ultimate load [mm]	1.02	13.7	34.3

4.2 Results Geometric Imperfections

As it became clear in the previous chapter, Modes 1 & 5 and 3 & 4 showed the following expected trends: with increasing amplitudes, their respective ultimate load decreases, while their stiffnesses remain equal to the baseline mode. Figures 4.2 and 4.3 compare the imperfect FE models with the *perfect* S4R baseline model and Panel 1 and 2 from Lanzi et al. [29].

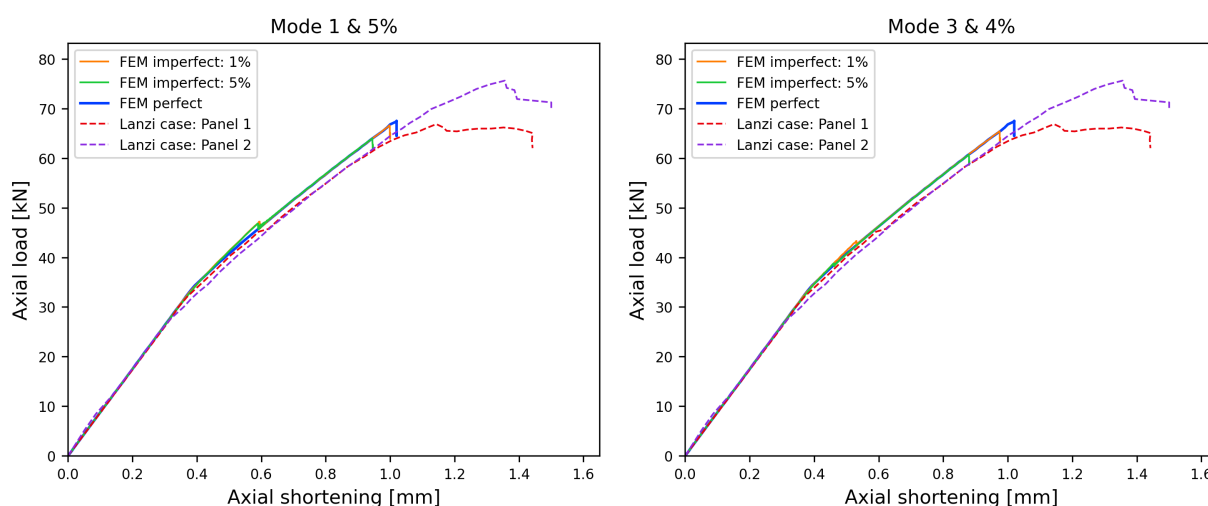


Figure 4.2: Mode 1 & 5 models compared with Panel 1 **Figure 4.3:** Mode 3 & 4 models compared with Panel 1 from the experiments by Lanzi et al. [29].

In both plots, all the curves show similar trends up until the first buckling load at an axial shortening value of around 0.4 mm. This behaviour was already expected upon reviewing the literature on the influence of imperfections on post-buckling. The transition into post-buckling is made visible for an amplitude of 1% (see Figure 4.4), with their average loads displayed at the top row. While the perfect baseline model transitions into five half-waves, the models with imperfections exhibit four half-waves in the vertical direction.

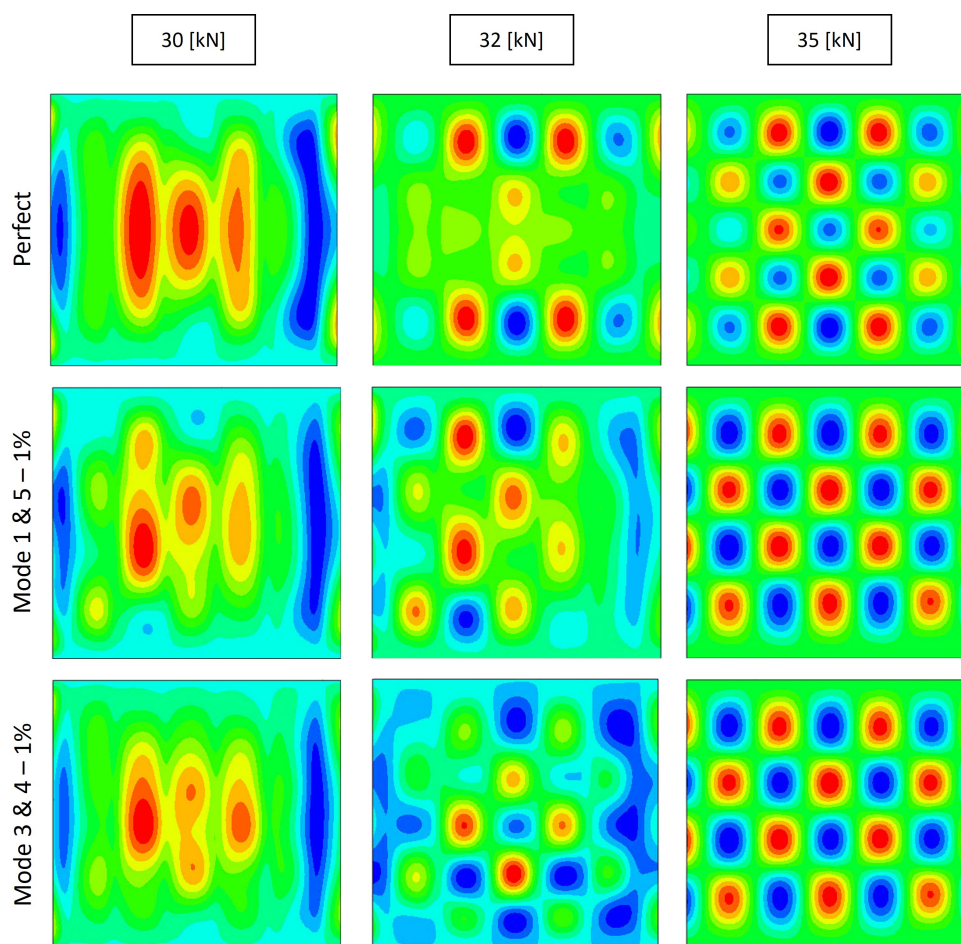


Figure 4.4: Transition from the pre-buckled state (far left) to the first-buckled state (far right) with increasing load. The top row displays their average loads.

Following these four half-waves, the models with imperfections exhibit a mode jump after a load drop to five half-waves in the vertical direction. These drops are visible in Figures 4.2 and 4.3. The model with imperfections (Mode 1 & 5) exhibits a sudden drop in load at approximately 0.6 mm for both amplitudes. A similar trend is observed for Modes 3 & 4, though it is less noticeable: at a 1% amplitude, this drop occurs around 0.6 mm, and for a 5% amplitude, it happens around 0.4 mm. These minor drops can be attributed to the eigenmode shapes and the amplitude used as a geometric imperfection, resulting in mode interaction that causes the load to drop. This transition of the panel from having four to five half-waves in the vertical direction is shown in the following figure.

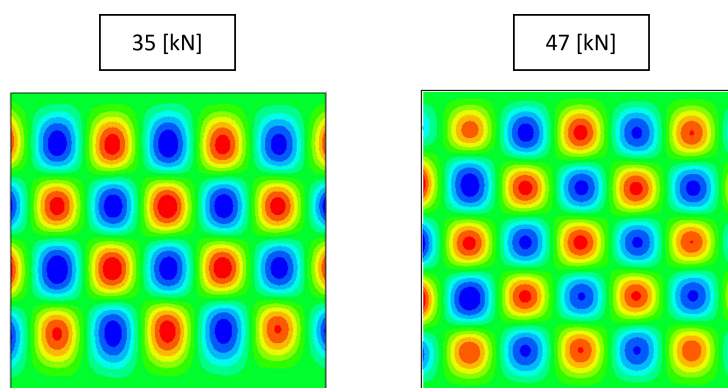


Figure 4.5: Mode transition from four to five half-waves in the vertical direction for an amplitude of 1%.

Apart from the small load drop, the stiffnesses remain consistent with the baseline model until reaching the ultimate load, where a decrease is observed in the ultimate load with increasing imperfection amplitude. This trend is supported by the findings of Lynch et al. [14], as discussed in Chapter 1, who also noted a decrease in ultimate load for increased imperfections amplitudes.

To discern the differences between the FE models and experimental data, the data is tabulated. Table 4.3 presents the perfect S4R model and the (absolute) deviation in percentages with respect to Panel 1 from the experiment of Lanzi et al. [29]. Panel 2 is excluded from this comparison, as Panel 1 demonstrates a better correlation with the FE model, as outlined in Section 4.1. The detailed data for Panel 1 and the corresponding FE models can be referenced in Appendix C for the sake of brevity.

Table 4.3: Comparison of Panel 1 from experimental data with baseline and imperfect S4R models, indicating their deviations (%).

Description	Baseline model	Mode 1 & 5		Mode 3 & 4	
		1%	5%	1%	5%
First buckling load [kN]	4.3%	1.8%	0.0%	1.2%	4.6%
Axial shortening at the first buckling load [mm]	0.0%	2.6%	2.6%	4.9%	7.7%
Initial stiffness [kN/mm]	5.0%	5.4%	3.4%	4.7%	4.2%
Ultimate load [kN]	1.2%	0.2%	4.0%	2.0%	9.0%
Axial shortening at the ultimate load [mm]	12.8%	14.5%	19.7%	16.8%	25.0%

Overall, Mode 1 & 5 with a 1% amplitude demonstrates the closest results to the experimental data. The introduction of imperfections leads to lower axial shortening when compared to Panel 1, as evident from the table. Although not shown in the table, it is worth noting that the FE model also exhibits lower axial shortening values than Panel 2. The difference in axial shortening between the FE models and the physical panels was initially observed with the baseline model and became even more pronounced with the addition of imperfections. This suggests that the imperfections lead to a stress redistribution in the panel and trigger mode jumps, which in turn lead to lower ultimate load with less axial shortening. If imperfec-

tions were to affect the shortening behaviour independently of the ultimate load, a change in stiffness relative to the baseline model would be expected to be observed.

As mentioned in Chapter 2, the FE models are not able to predict failure modes like crippling, which is activated when stress surpasses a certain threshold during a load drop. This was also supported by literature: Perret et al. [44], for example, observed delamination at the load drop, which was initiated by crippling. Therefore, beyond the load drop, the present study is limited to predicting failure modes.

Finally, the out-of-plane displacements are displayed in Figure 4.6. Taking the imperfection amplitude of 1% of the thickness, there is a decrease in the maximum out-of-plane displacement for positive displacements at the ultimate load. Conversely, there is an increase in the maximum out-of-plane displacement for negative displacements. Note again: Negative values indicate outward displacement, whereas positive values represent inward displacement with respect to the panel's surface. The differences observed in the displacements are the results of the eigenmodes selected as an initial condition. In particular, the imperfection using Modes 3 & 4 exhibits a closer alignment with the experiment: a deviation of 7.7% for the max and 1.7% for the minimum value. Amplitudes higher than 1% lead to more pronounced decreases in the ultimate loads and greater deviations in their out-of-plane displacements from Panel 1. Therefore, higher amplitudes do not necessarily correlate with increased out-of-plane displacements at the ultimate load.

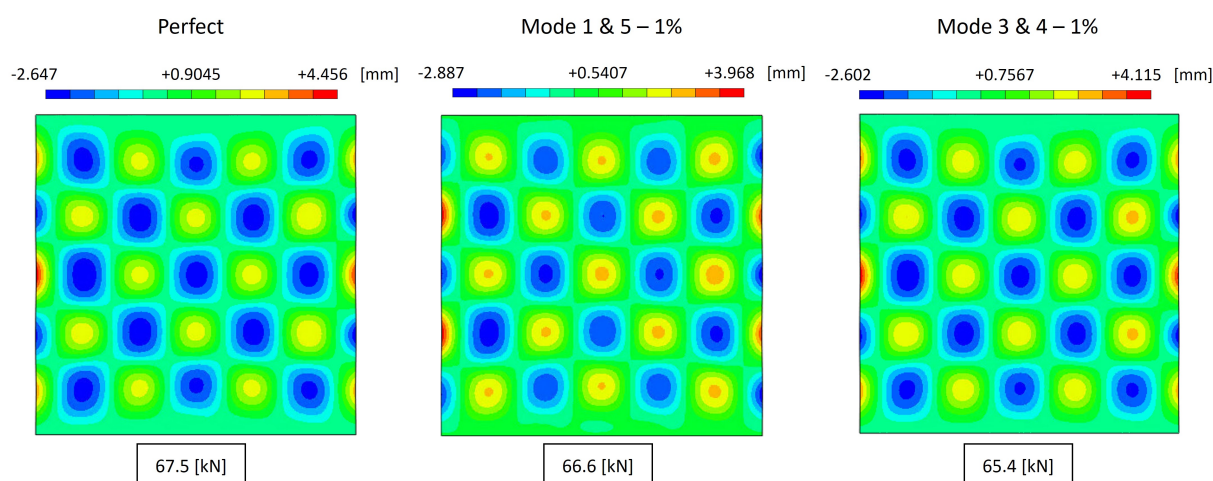


Figure 4.6: Maximum out-of-plane displacement for the ultimate load.

The variation observed in out-of-plane displacements appears to be a direct result of the selected imperfection pattern. Given that these patterns are derived from linear buckling modes, which closely resemble the post-buckled configuration, the amplitude differences may well be attributed to the constructive or destructive interference of the buckling modes while being superimposed and giving rise to nonlinear buckling patterns. This interplay indicates that the choice of imperfection pattern influences the structural response, highlighting the critical role of accurately capturing and representing these imperfections in predictive modelling.

4.3 Results Loading Imperfections

Similarly to geometric imperfections, the existence of loading imperfections in the experiments of Lanzi et al. cannot be inferred from the published data. From the literature, it was understood that Park et al. [26] explored the influence of loading imperfections by placing the loading plate at a tilted angle in their simulations. The results obtained in this study will be first compared with data from Lanzi et al. and, subsequently, examine how these trends align with the work by Park et al.

In Chapter 3, it was observed that applying the loading plate in the SC8R models toward the back and front edges of the plate (refer to Figure 3.13 for the orientation) did not significantly alter the results. As demonstrated in the subsequent figure, except for a minor load drop at approximately 0.6 mm of axial shortening, the patterns observed closely align with those from the perfect baseline case.

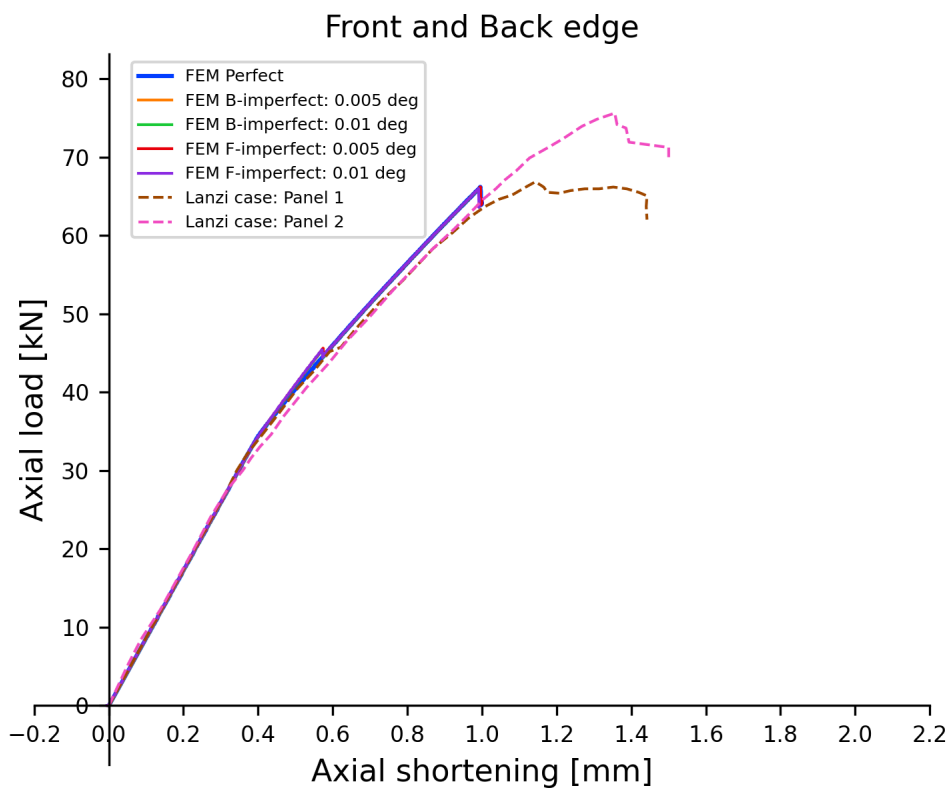


Figure 4.7: Back (B) and Front (F) edge configurations.

On the other hand, the tilted configurations on the Left- and Right edges of the stiffened panel did affect the results. For this reason, only these configurations are considered here. The graphs for both configurations, with their respective tilted angles, are presented alongside Panel 1 and 2 in Figures 4.8 and 4.9 respectively.

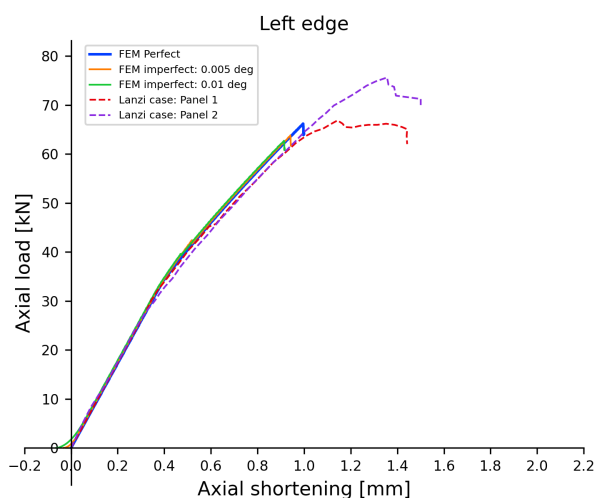


Figure 4.8: SC8R Left edge configuration.

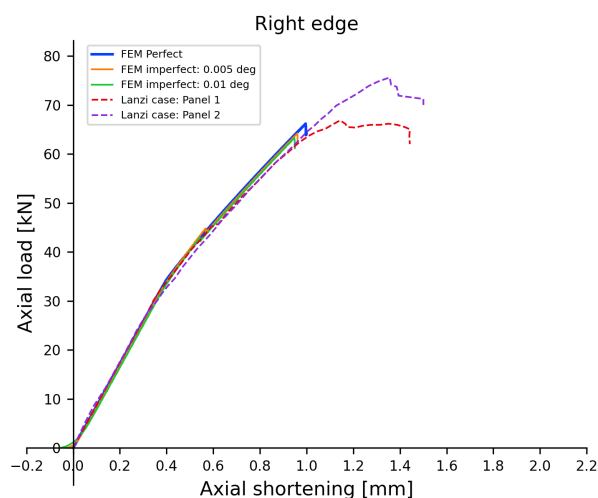


Figure 4.9: SC8R Right edge configuration.

Recalling from Chapter 3, the loading plate was positioned with an offset from the stiffened panel. This is evident in the negative axes since the displacement is measured in the mid-section of the loading plate. In the tilted configuration, one part of the stiffened panel initiates contact first with the loading plate. Figures 4.8 and 4.9 back this reasoning, given their similar load-shortening trend to that of the baseline model. The differences in results due to left and right tilted planes are expected, stemming from the panel's design, where the right side has a stiffener closer to the edge. This asymmetrical placement of the stiffeners naturally leads to varying responses under the applied loads. A correlation is also visible compared to the study by Park et al. [26]. In their research, a closer relation to experimental results was observed in terms of stiffness behaviour for a tilted loading plate (see Figure 1.10).

Both figures demonstrate a good alignment up to 0.4 mm, marking the onset of the initial buckling. It is interesting to note how the 0.01-degree option exhibits a higher offset in the left plot and a lower offset in the right plot compared to Panel 1. The left figure also clearly shows the slightly reduced overall stiffness for the baseline model. This phenomenon was previously attributed to the contact formulation, which introduces extra compliance through a default artificial contact stiffness, reducing overall stiffness, as detailed in Section 3.2.

Reduced ultimate loads are observed with increased tilted angle. Similar to models with geometric imperfections, the loading imperfections can trigger mode jumps, leading to lower ultimate load, with decreased axial shortening.

In the figures below, the pre-buckling transition is shown for 0.005 deg since 0.01 deg shows similar patterns. A clear difference is visible between the panels in terms of where the loading plate first comes into contact with the panel. For completeness, it is important to mention that the data is read manually, and the modes are not captured exactly. Therefore, they do not show identical patterns with respect to each other.

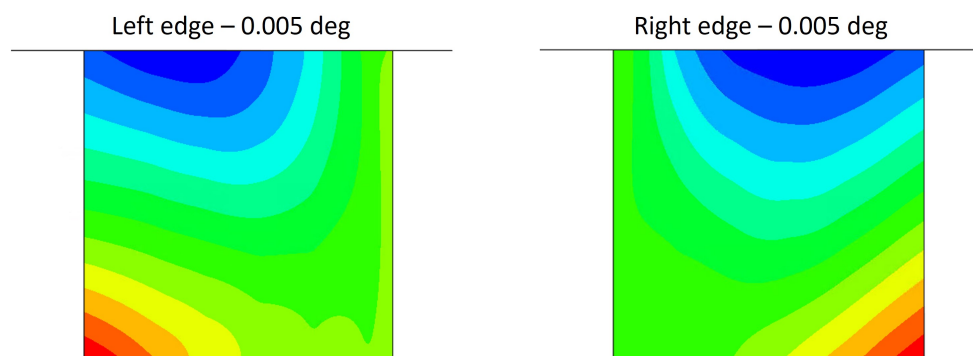


Figure 4.10: Transition mode into post-buckling.

After the transition from pre-buckling into post-buckling, the panels show the same buckling pattern as visible in Figure 4.11. The panels switch modes right after the first buckling mode, which is made visible on the right. This is possibly due to the modes being close to each other and the five half-waves dominating the physical realm.

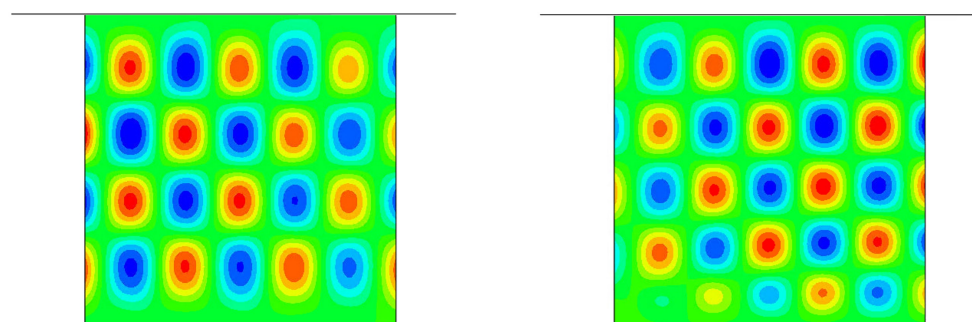


Figure 4.11: Transition from four half-waves in the vertical direction to five half-waves.

Overall, the main differences were observed at first initial contact, the offset from the baseline model (resulting from the initial contact) and the change in ultimate loads. One factor not discussed yet is the out-of-plane displacement. Park et al. [26] note in their work that they have observed comparable out-of-plane displacements to experiments but with increased non-linear deformations. In the present study, similar magnitudes of out-of-plane displacements in both the baseline (Figure 2.14) and models with loading imperfections (Figure 4.12) are observed. This suggests that loading imperfections might not significantly affect their out-of-plane behaviour. When it comes to the increased nonlinear deformations observed in the work of Park et al., it is challenging to make a clear statement in the present study. To do so, as previously mentioned, clarity in the exact experimental conditions is necessary. Only speculations can be made regarding how these trends might compare to data from Lanzi et al. [29]. Additionally, an axial compression test, as described in Section 2.1, needs to be conducted again to clearly measure the tilted position of the loading plates. This measurement can be done using LVDT sensors, as also reflected later in this thesis, in the recommendations section.

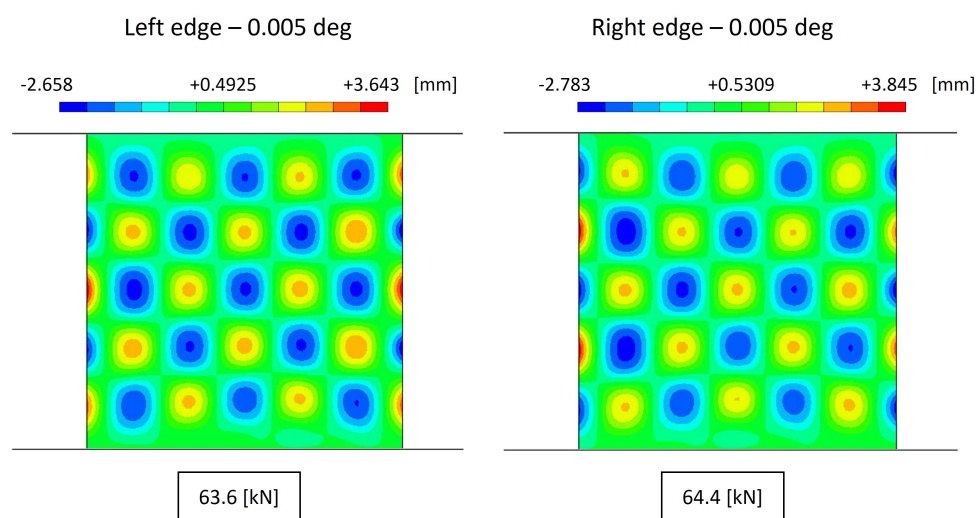


Figure 4.12: Out-of-plane displacement for the Left- and Right-edge configurations.

4.4 Discussion

Beginning with the experimental data from Lanzi et al., as explained in Chapter 2, the discrepancy in results (12% difference in their ultimate loads) for theoretically similar panels was attributed to variations in the collapse mode. This is very likely given that the baseline model matched more closely with Panel 1. The difference in collapse modes is because of the panel's behaviour. In Chapter 2, the findings from Lanzi et al. [29] were discussed regarding this behaviour: they noted that for Panel 1, the skin bent away from the flange, and failure was observed halfway through the web height of the stiffener, where the higher bending stresses of the stiffener were located. Ultimately, this results in the crippling of the web. Conversely, for Panel 2, failure was observed at both the top and bottom parts of the stiffener web, with the skin bending towards the stiffened side. The fillet of the stiffener could possibly fail due to material failure. However, it is more likely that the top part of the stiffener web failed due to crippling in between two sets of rivets as suggested by the high compressive stresses in this region in Figure 2.10.

Another noteworthy point is the observed sudden displacement difference between the tested panels in the region of 0.4 and 0.6 mm approximately. Since the first buckling happens at 0.4 mm, the change in stiffness of the panels is attributed to post-buckling. The baseline models, on the other hand, show a continuous steady stiffness. Referring back to the models with imperfections in the previous sections, a small load drop was visible in a region similar to Panel 1. It was assumed that this was attributed to a small mode transition. Upon inspecting the behaviour observed between Panel 1 and 2, it becomes evident that introducing imperfections brings the models closer to the experimental cases. Panel 2 does not show this load drop, so it's assumed that in the case of Panel 1, some imperfections were present in the form of geometric defects. Regarding the presence of loading imperfections, it is harder to make a statement since the experimental conditions are unknown. As for the buckling modes of Panel 2, since these are not available, it is still a challenge to make any further inferences regarding the post-buckling difference compared to Panel 1.

As highlighted throughout this thesis, the FE models do not account for failure, making them

less realistic after the sudden load drop. In real-world scenarios with physical panels, when a stiffener fails, the structure redistributes the loads to the remaining stiffeners until the panel reaches its ultimate collapse point.

The common detail between all models with imperfections is their influence on buckling shapes upon transitioning from the first buckling mode to post-buckling modes and the decrease in their ultimate loads. This again highlights the close correlation with the observations made in the literature in the case of geometric imperfections. Also, the included eigenmodes (both first and higher modes) from the eigenvalue analysis for the geometric imperfections were mainly present in the panel's skin. This is logical, as the stiffeners are designed to counteract this out-of-plane behaviour. The eigenmodes depicted in this thesis emphasise solely the out-of-plane displacement in the skin, as their magnitude substantially surpasses that observed in the stiffeners.

One type of geometric defect that could have resulted in stiffness reduction is introducing geometric imperfect stiffeners. The study by Prato et al. [15] included uneven stiffener length compared to the skin, resulting in stiffness differences in the post-buckled region. It is believed that adding such imperfections to the present model would decrease the ultimate load even further and could also result in stiffness loss since the stiffeners are the main load carriers in the post-buckling region.

Models with loading imperfections exhibit similar behaviour to what was observed for the ones with geometric imperfections: with increasing tilted angles, their ultimate loads decrease. In addition to this, the structure loses possibly a certain amount of stiffness, given that a part of the structure is loaded earlier and encounters higher stresses. This results in an offset in the load-shortening results. Also, the design of the structure is highly relevant: here, the right segment of the panel, where stiffeners are closer to the edge, showed a better resistance for non-uniform loading since the stiffeners carry more loads. One aspect not addressed in the previous chapters is the use of carriage guides by Lanzi et al. to prevent non-uniform loading. An often overlooked consideration is that such a system does not directly establish uniform contact with the panel. The current thesis substantiates this by demonstrating that initial load application at an angled position unveils variations when compared to the baseline model.

The perfect baseline model showed a transition to five half-waves (vertical direction) upon entering post-buckling. The models with imperfections first showed four half-waves in the vertical direction, followed by five. However, this buckling pattern cannot be exactly validated as the experimental data for these loads (between 30-35 kN) are unavailable.

Failing to include actual potting may impact the variance between the shape changes observed in the FE model and the experiment. For instance, models with loading imperfections demonstrate a smooth transition from four to five half-waves, whereas those based on geometric imperfections undergo a more abrupt change. This could be due to the gradual transfer of load in the case of loading imperfections. The sudden shift observed in geometric models can be attributed to the absence of potting.

5

Conclusion

The main objective of this thesis was to systematically show the influence of geometric and loading imperfections on the onset of buckling and post-buckling behaviour of an L-stiffened composite panel using finite elements. In the following concluding section, the fulfilment of this research objective is discussed by self-reflecting on the research questions and hypotheses of this thesis, followed by concluding remarks.

5.1 Reflection on Research Questions

A main research question, presented below, was formulated based on the thesis objective, accompanied by sub-questions and hypotheses (repeated from Chapter 1) to answer the main question.

Main research question:

What is the influence of geometric and loading imperfections on the post-buckling behaviour of L-stiffened composite panels?

Sub-question 1

Which buckling modes can be employed to more accurately represent the geometrical imperfections and observe responses according to experimental data?

Hypothesis 1 stated the following:

The literature [19, 22] has presented strategies that include the use of eigenmodes from the linear eigenvalue analysis for geometric imperfections. Based on these studies, this thesis hypothesised that the first modes of the eigenvalue analysis will generate more representative results than higher modes close to the ultimate load.

Hypothesis 1 - Disproved

In the present thesis, both first modes as well as higher modes (close to the ultimate load), showed representative results. It is important to consider combinations of modes with shapes and amplitudes that can more accurately represent the experimental geometric imperfection patterns, and that are capable of triggering the same post-buckling mechanisms as the real imperfections.

Sub-question 2

How can loading imperfections be modelled effectively to align the responses of the FE model with experimental data?

Hypothesis 2 stated the following:

In this thesis, it was hypothesised that loading imperfections through the tilted angle approach, as suggested by Park et al. [26] can accurately represent the experimental data.

Hypothesis 2 - Proved

The thesis has adopted the tilted angle approach, and this resulted overall in good agreement with the results from Lanzi et al. and Park et al. in terms of stiffness trends and the behaviour of the ultimate loads, that decreased with increasing tilt angles.

Sub-question 3

How do geometrical and loading imperfections influence the onset of buckling and the post-buckling?

Hypothesis 3 stated the following:

For geometric imperfections, it could be inferred from the literature [14, 24] that they have an influence on the ultimate load. Hence, in this thesis it was hypothesised that the geometric imperfections will only influence the ultimate load for the L-stiffened panel model. This is also hypothesised for the loading imperfections. In addition to this, based on the work of Park et al. [26], it is expected that a similar offset trend is going to be observed from the experimental data.

Hypothesis 3 - Proved

Prior to the first buckling load, both types of imperfections did not show any effect. The post-buckling is affected by both types of imperfections, which are mainly visible in the ultimate load and when local buckling switches to global buckling / post-buckling.

5.2 Concluding Remarks

The present study on the influence of geometric and loading imperfections on post-buckling behaviour has yielded several insightful conclusions. Regarding geometric imperfections, the analysis revealed that different eigenmode shapes and amplitudes significantly impact behaviour beyond the first buckling load. Some configurations exhibited small mode jumps due to mode interaction, whilst others did not display such behaviour. A key observation was the variance in ultimate load: at higher amplitudes some modes intuitively resulted in lower ultimate loads, while some showed counter-intuitive results with increased loads. This emphasises the crucial need for the careful selection of the appropriate eigenmode shape and amplitude to accurately represent geometric imperfections in post-buckling behaviour.

Similarly, loading imperfections demonstrated behaviours akin to those of geometric imperfections, notably affecting the ultimate loads. Beyond this, they also introduced an offset in the load-axial shortening behaviour from the perfect baseline model, dependent on the specific configuration and tilt angle. Based on these observations, it can be concluded that their influence should be accounted for.

In summary, this study highlights the importance of a detailed and meticulous approach in the selection and incorporation of both geometric and loading imperfections in structural modelling. In the case of geometric imperfections, both first and higher eigenmodes can represent the geometric imperfections. As for loading imperfections, the configurations where the loading plate tilted towards the left- and right edge resulted in a significant difference with respect to the baseline model. Acknowledging and including these imperfections is crucial for a more realistic representation of post-buckling behaviour and for accurately predicting ultimate load capacities.

Recommendations

This chapter provides a brief overview of the primary recommendations for the future continuation of this research project.

Material and Crippling Failure

In the FE models, to test the hypothesis regarding the onset of crippling following the load drop, the Tsai-Hill criterion was examined for material failure. However, the failure index never reached "1" even after the load drop, suggesting that no failure had occurred. A more realistic failure model would incorporate the following aspects:

- Include cohesive zones in the model to account for debonding between the skin and the stiffener, as well as for delaminations,
- Implement a material model such as the Hashin [39], or LaRC05 [45] criteria, with progressive damage evolution to account for material degradation in highly stressed regions.

Joint Approximation

The influence of the rivets joining the stiffeners to the skin was not considered in the FE models. Literature does suggest that modelling these joints can affect the results. For future studies, the influence of rivets can be modelled by introducing their residual stresses, as also suggested by Lynch et al. [14].

Test Methodology Loading Imperfection

Creating validated FE models is highly relevant as it facilitates further exploration of a given design space. A typical process prior to an experiment commences with the generation of an FE model to predict the panel's response. Subsequent to this, the tests are performed, followed by the validation of the FE model.

The conditions for such tests are not always ideal. To understand the deviations in post-testing results, it is essential to include certain imperfections in the FE model. This thesis has addressed this by introducing both geometric and loading imperfections. By validating the FE model and comparing it with models that contain these imperfections, the variations in results can be logically explained.

In the experimental phase, beyond the standard procedure of measuring geometric imperfections, it is also necessary to capture loading imperfections. This allows for a comparison

with the outcomes from models that incorporate these imperfections, thereby validating the approach of measuring the tilted angle. Naturally, once such data is obtained, it can be directly integrated into the analysis and used to assess the method's precision.

For conducting the axial compression test, the equipment available at the Aerospace Faculty of TU Delft can be utilised, as illustrated in the subsequent figure.



Figure 6.1: The mechanical testing setup to use for axial compression testing.

Two measurements for loading imperfections need to be considered for the experiment:

- Measuring the deformations in the loading plate.
- Measuring the tilted angle of the loading plate during the test.

The former can be accomplished using the FARO Gage measuring arm, a commercial brand utilised to measure the existing deformations in the panel before testing. Additionally, two DIC (Digital Image Correlation) cameras can measure these deformations and capture the buckling behaviour of the panel. Although the stiffeners have an open section, it is recommended to position the DIC cameras on the unstiffened side of the panel to fully capture the buckling behaviour.

Since the setup has four corners, it is necessary to employ four LVDT (Linear Variable Differential Transformer) sensors, one for each corner, to measure the tilted angle of the loading plate with respect to the panel. These measurements are essential to validate the modelling

approach adopted in this thesis for loading imperfections. In addition, the LVDTs need to be placed close to the panel as well to make sure their axial shortening is measured.

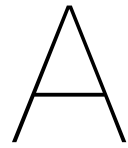
During the experiment, one of the main objectives is to record the failure. For this, a minimum of two high-speed cameras should be installed on the stiffened side, positioned at an angle to accurately capture the initial failure in the panel. At least two are required to ensure visual coverage of the test specimen during testing. This is necessary because certain parts of the specimen may be obscured from the view of one camera due to its positioning.

References

- [1] Candelaria Bergero et al. “Pathways to net-zero emissions from aviation”. In: *Nature Sustainability* 6.4 (2023), pp. 404–414.
- [2] Richard Degenhardt et al. “COCOMAT—improved material exploitation of composite airframe structures by accurate simulation of postbuckling and collapse”. In: *Composite Structures* 73.2 (2006), pp. 175–178.
- [3] Jakob C Schilling and Christian Mittelstedt. “Local postbuckling of omega-stringer-stiffened composite panels”. In: *Thin-Walled Structures* 181 (2022), p. 110027.
- [4] Riccardo Vescovini, Carlos G Davila, and Chiara Bisagni. *Simplified Models for the Study of Postbuckled Hat-Stiffened Composite Panels*. Tech. rep. 2012.
- [5] Giulio Romeo and Giacomo Frulla. “Post-buckling behaviour of graphite/epoxy stiffened panels with initial imperfections subjected to eccentric biaxial compression loading”. In: *International journal of non-linear mechanics* 32.6 (1997), pp. 1017–1033.
- [6] Riccardo Vescovini and Chiara Bisagni. “Two-step procedure for fast post-buckling analysis of composite stiffened panels”. In: *Computers & Structures* 128 (2013), pp. 38–47.
- [7] Christian Mittelstedt and Matthias Beerhorst. “Closed-form buckling analysis of compressively loaded composite plates braced by omega-stringers”. In: *Composite Structures* 88.3 (2009), pp. 424–435.
- [8] Ramesh Chandra. “Postbuckling analysis of crossply laminated plates”. In: *AIAA Journal* 13.10 (1975), pp. 1388–1389.
- [9] M Beerhorst, M Seibel, and C Mittelstedt. “Fast analytical method describing the postbuckling behavior of long, symmetric, balanced laminated composite plates under biaxial compression and shear”. In: *Composite Structures* 94.6 (2012), pp. 2001–2009.
- [10] A. Milazzo and V. Oliveri. “Buckling and postbuckling of stiffened composite panels with cracks and delaminations by ritz approach”. In: *AIAA Journal* 55 (3 2017), pp. 965–980. DOI: 10.2514/1.3055159.
- [11] Saullo GP Castro and Mauricio V Donadon. “Assembly of semi-analytical models to address linear buckling and vibration of stiffened composite panels with debonding defect”. In: *Composite Structures* 160 (2017), pp. 232–247.
- [12] Kai Steltner, Benedikt Kriegesmann, and Claus BW Pedersen. “Robust sizing optimization of stiffened panels subject to geometric imperfections using fully nonlinear postbuckling analyses”. In: *Thin-Walled Structures* 175 (2022), p. 109195.
- [13] Mariano A Arbelo, Sérgio Frascino M de Almeida, and Maurício V Donadon. “An experimental and numerical analysis for the post-buckling behavior of composite shear webs”. In: *Composite structures* 93.2 (2011), pp. 465–473.
- [14] C Lynch et al. “The computational post buckling analysis of fuselage stiffened panels loaded in compression”. In: *Thin-walled structures* 42.10 (2004), pp. 1445–1464.
- [15] A Prato et al. “Buckling and post-buckling of thin-walled stiffened panels: modelling imperfections and joints”. In: *Thin-Walled Structures* 172 (2022), p. 108938.
- [16] Carlos Couto et al. “Effective width method to account for the local buckling of steel thin plates at elevated temperatures”. In: *Thin-Walled Structures* 84 (2014), pp. 134–149.
- [17] Adib Abdulghafour Becker. *Understanding non-linear finite element analysis through illustrative benchmarks*. NAFEMS, 2001.

- [18] Saullo GP Castro et al. "Geometric imperfections and lower-bound methods used to calculate knock-down factors for axially compressed composite cylindrical shells". In: *Thin-Walled Structures* 74 (2014), pp. 118–132.
- [19] S Farzarian et al. "Geometric imperfections in CFS structural members: Part I: A review of the basics and some modeling strategies". In: *Thin-Walled Structures* 186 (2023), p. 110619.
- [20] Benjamin W Schafer and Teoman Peköz. "Computational modeling of cold-formed steel: characterizing geometric imperfections and residual stresses". In: *Journal of constructional steel research* 47.3 (1998), pp. 193–210.
- [21] Leroy Gardner. "A new approach to structural stainless steel design". In: (2002).
- [22] Chiara Bisagni and Carlos G Dávila. "Experimental investigation of the postbuckling response and collapse of a single-stringer specimen". In: *Composite Structures* 108 (2014), pp. 493–503.
- [23] Damodar R Ambur, Navin Jaunky, and Mark W Hilburger. "Progressive failure studies of stiffened panels subjected to shear loading". In: *Composite structures* 65.2 (2004), pp. 129–142.
- [24] AC Orifici et al. "Degradation investigation in a postbuckling composite stiffened fuselage panel". In: *Composite Structures* 82.2 (2008), pp. 217–224.
- [25] Kevin van Dooren and Chiara Bisagni. "Design, analysis and testing of thermoplastic welded stiffened panels to investigate skin-stringer separation in post-buckling". In: *Composites Part B: Engineering* 267 (2023), p. 111033.
- [26] Oung Park et al. "Analytical-experimental correlation for a stiffened composite panel loaded in axial compression". In: *Journal of aircraft* 38.2 (2001), pp. 379–387.
- [27] Somanath Nagendra et al. "Improved genetic algorithm for the design of stiffened composite panels". In: *Computers & Structures* 58.3 (1996), pp. 543–555.
- [28] Mark William Hilburger. *Numerical and experimental study of the compression response of composite cylindrical shells with cutouts*. University of Michigan, 1998.
- [29] Luca Lanzi and Chiara Bisagni. "Post-Buckling experimental tests and numerical analyses on composite stiffened panels". In: *44th AIAA/ASME/ASCE/AHS/ASC Structures, Structural Dynamics, and Materials Conference*. 2003, p. 1795.
- [30] Luca Lanzi. "Composite stiffened panels in postbuckling: experiments and dynamic explicit analyses with LS-DYNA". In: (2004).
- [31] Luca Lanzi. "An experimental investigation on the post-buckling behavior of composite stiffened panels". In: *45th AIAA/ASME/ASCE/AHS/ASC Structures, Structural Dynamics & Materials Conference*. 2004, p. 1566.
- [32] Luca Lanzi. "A numerical and experimental investigation on composite stiffened panels into post-buckling". In: *Thin-walled structures* 42.12 (2004), pp. 1645–1664.
- [33] Simulia. *ABAQUS/Standard User's Manual 2023*. URL: <https://help.3ds.com/>.
- [34] JC Roberts et al. "Buckling, collapse and failure analysis of FRP sandwich panels". In: *Composites Part B: Engineering* 33.4 (2002), pp. 315–324.
- [35] C Williamson and SJ Lord. "Damage Prediction and its Effect on Post-Buckled Wing Design". In: *2nd International Conference on Buckling and Postbuckling Behaviour of Composite Laminated Shell Structures, Braunschweig, Germany*. Citeseer. 2008.
- [36] Andrea Faggiani and Brian G Falzon. "Optimization strategy for minimizing damage in postbuckling stiffened panels". In: *AIAA journal* 45.10 (2007), pp. 2520–2528.
- [37] Carlos G Dávila and Chiara Bisagni. "Fatigue life and damage tolerance of postbuckled composite stiffened structures with initial delamination". In: *Composite Structures* 161 (2017), pp. 73–84.

- [38] Kuo-Shih Liu and Stephen W Tsai. "A progressive quadratic failure criterion for a laminate". In: *Failure Criteria in Fibre-Reinforced-Polymer Composites*. Elsevier, 2004, pp. 334–352.
- [39] Zvi Hashin. "Fatigue failure criteria for unidirectional fiber composites". In: *Journal of applied mechanics* 47.4 (1980), pp. 329–334.
- [40] Alfred Puck. *Festigkeitsanalyse von Faser-Matrix-Laminaten: Modelle für die Praxis*. Hanser, 1996.
- [41] Christos Kassapoglou. *Design and analysis of composite structures: with applications to aerospace structures*. John Wiley & Sons, 2013.
- [42] Charlotte Mercier et al. "Analysis of the global and local imperfection of structural members and frames". In: *Journal of Civil Engineering and Management* 25.8 (2019), pp. 805–818.
- [43] David Bushnell et al. "Optimization of stiffened panels in which mode jumping is accounted for". In: *38th Structures, Structural Dynamics, and Materials Conference*. 1997, p. 1141.
- [44] Adrien Perret et al. "Global behaviour of a composite stiffened panel in buckling. Part 2: Experimental investigation". In: *Composite structures* 94.2 (2012), pp. 376–385.
- [45] ST Pinho et al. "Material and structural response of polymer-matrix fibre-reinforced composites". In: *Journal of Composite Materials* 46.19-20 (2012), pp. 2313–2341.



Baseline Configurations

This chapter presents some of the attempted alternative configurations before the baseline model is established, explained in Chapter 2. The focus is on the S4R element models because they exhibited behaviour similar to SC8R element-containing models while being more computationally efficient. The mesh convergence- and displacement rate convergence studies are also presented.

A.1 Stiffener Without Fillet- and Potted model

One iteration involved a stiffener without a fillet: from now on referred to as a fillet-less stiffener. This particular variant was chosen to simplify the model, since by considering a stiffener without a fillet, the computational complexity was reduced.

Another iteration was regarding the use of potting material. As explained in Chapter 2, it was unclear if the provided geometry by Lanzi et al. was within the clamping system or not. One possibility considered in this research is the inclusion of potting material at the top and bottom edges of the pane. Two options exist for including potting: physically modelling the potting material, or applying appropriate boundary conditions to the concerned region. The latter is preferred because of the lack of information on the potting material. The nodes are constrained in the out-of-plane ($U3$) and in-plane transverse direction ($U1$); see Figure A.1 where the grey area represents the potted region. This approach was also found to be used in the study of Park et al. [26]. To determine the potted area, the pixels in the experimental setup image of the Lanzi case were counted: an area roughly 50 mm away from both the top and bottom edges was estimated.

The fillet-less stiffener model and the potted model are then compared with the final baseline model, which contains stiffeners with fillet and not potted regions. The final baseline model signifies the validated baseline model representing the Lanzi case and is detailed in Chapter 2.

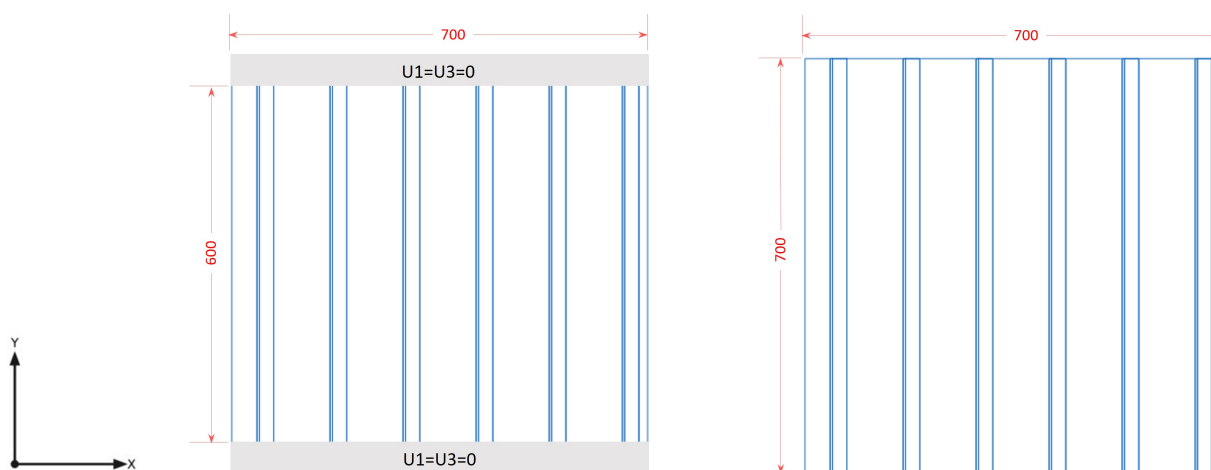


Figure A.1: On the left, the potential potted area is visible (not to scale), while on the right, it is shown without potting.

In Figure A.2, the first buckling mode from the linear eigenvalue analysis is compared for each design.

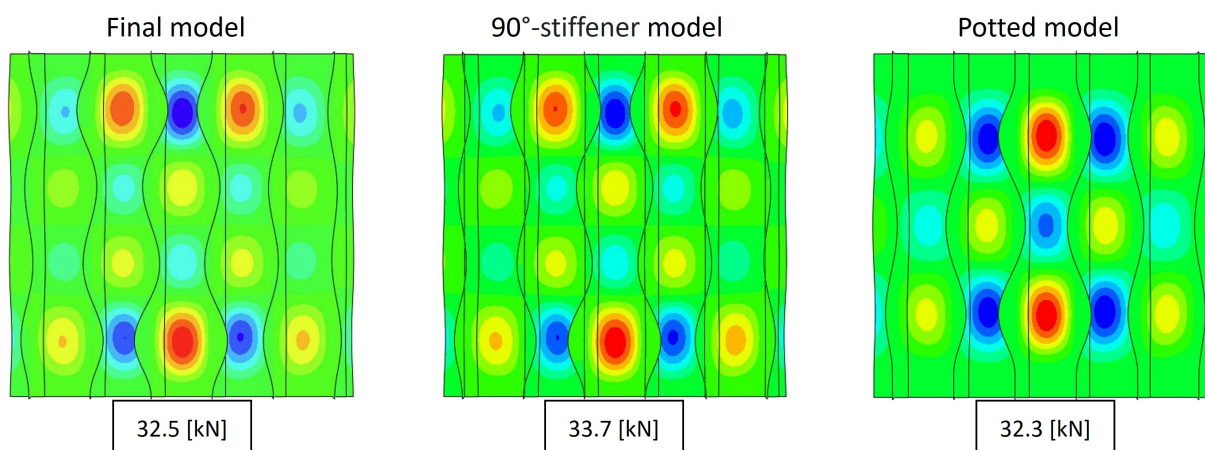


Figure A.2: Comparison of the first mode of the final, fillet-less stiffener and potted models - a scaling factor of 50% is applied.

The fillet-less stiffener model does not show a significant difference, whereas, for the potted model, the modes have shifted more to the centre. This was expected with the additional constraints used to simulate potted area.

The differences are also visible in Figure A.3, where the ultimate load is close to 85 kN for the potted model, significantly higher than for the other two models. As for the fillet-less stiffener, it shows an increased stiffness compared to the other two designs, which is expected since the stiffeners have more contact area with the skin. For that reason, this option was also disregarded as it clearly shows a difference with a stiffener, including a fillet.

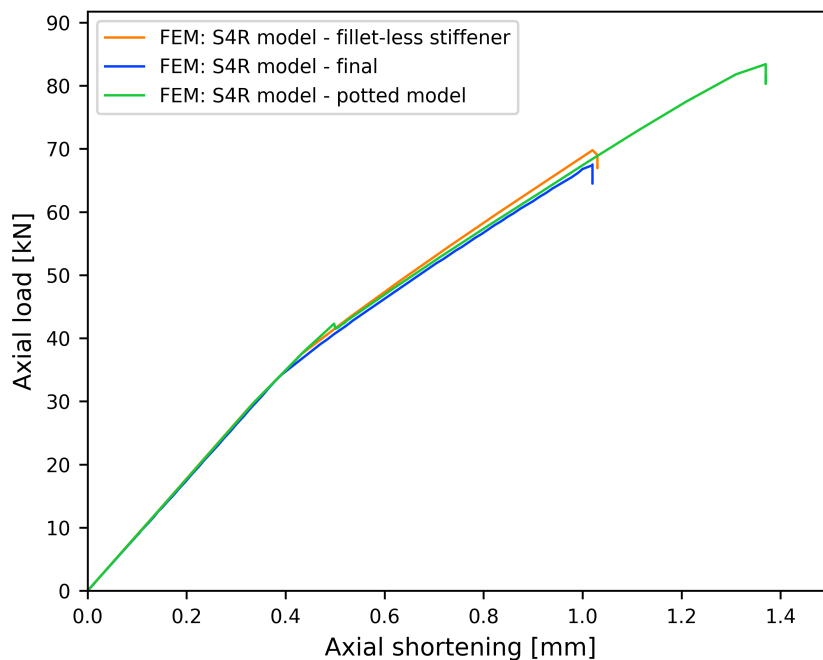


Figure A.3: The final selected model is compared with a model containing fillet-less stiffeners and a potted model.

A.2 Mesh convergence study

As highlighted in Chapter 2, a convergence analysis was conducted before settling on a mesh size of 5 mm x 5 mm. Mesh sizes of 10x10, 8x8, and 5x5 were tried, revealing negligible differences beyond the 5x5 configuration. Figure A.4 illustrates the comparison between the 8x8 and 5x5 mesh sizes, demonstrating nearly identical trends, with only a slight variance observed in the ultimate load.

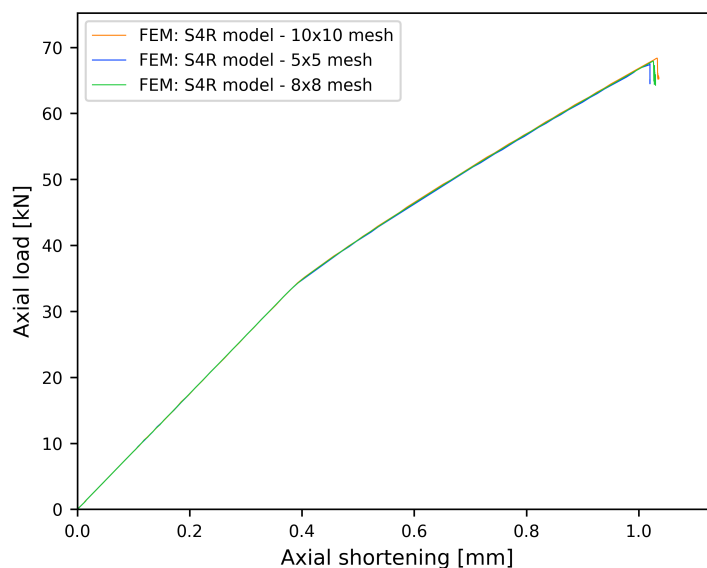


Figure A.4: Comparison of the mesh sizes.

A.3 Displacement rate convergence study

The study conducted on displacement rates is depicted in Figure A.5. It is evident that higher velocities result in numerical instability and convergence problems. This effect is even more pronounced when comparing the model with displacements of 0.26 mm/s and 0.13 mm/s (corresponding to the final baseline model labelled as *FEM: S4R model*) in Figure A.6. At first sight, no difference is visible. However, the detailed view on the right (Figure A.6) shows that the graph with 0.26 displays some fluctuation.

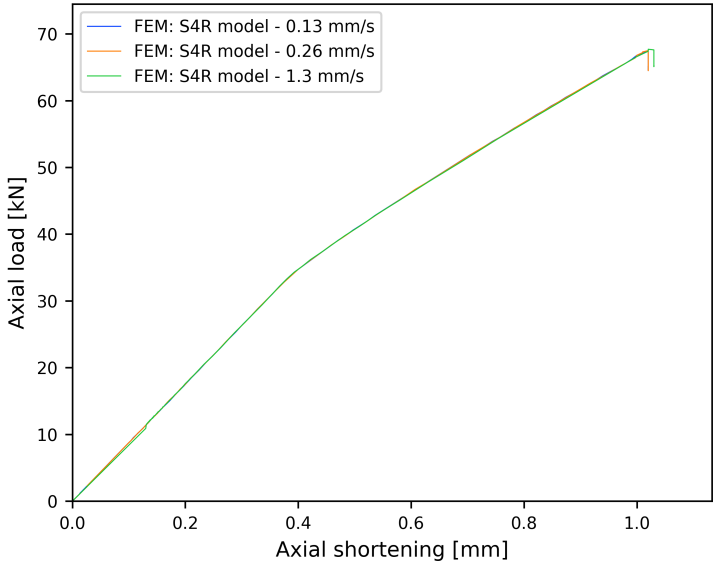


Figure A.5: Comparison of models with different displacement rates (final baseline model labelled as *FEM: S4R model* with a rate of 0.13 mm/s).

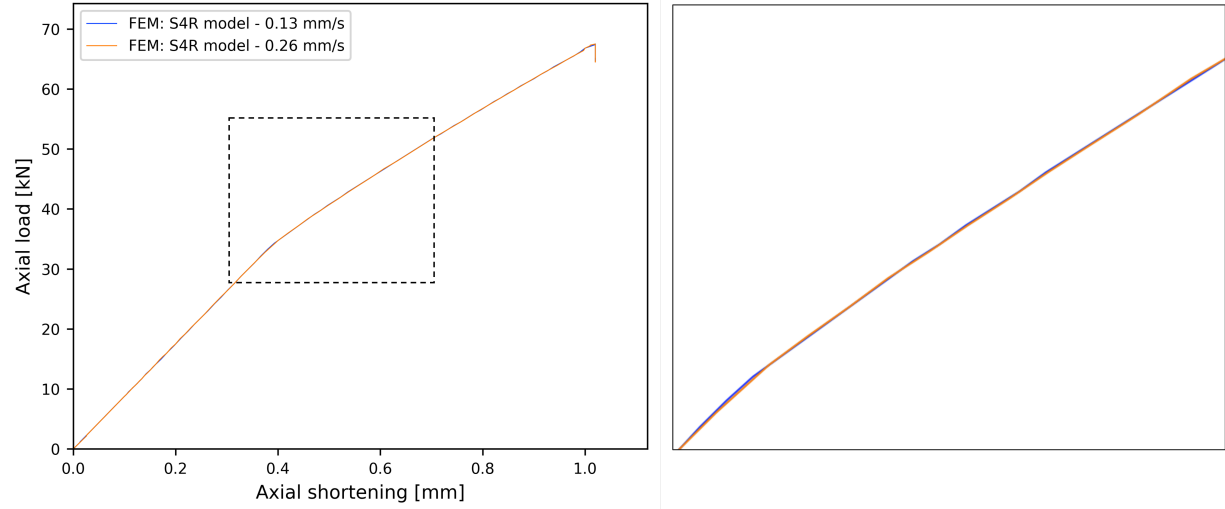


Figure A.6: Comparison of final baseline model labelled as *FEM: S4R model* with a rate of 0.13 mm/s and model with a rate of 0.26 mm/s.

B

Additional Imperfection Data

The following figures display the plots where all the considered imperfection amplitudes are included.

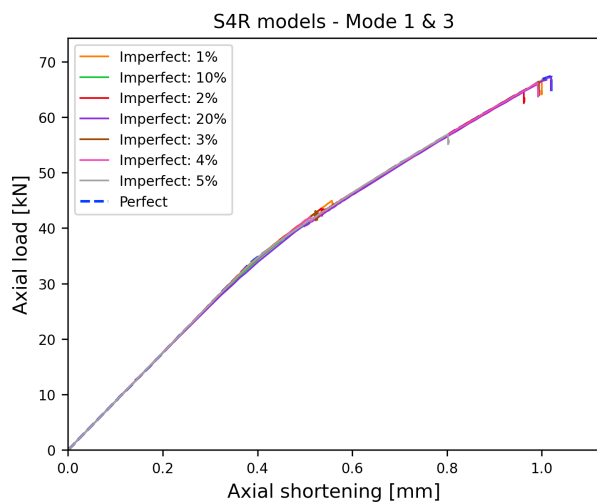


Figure B.1: S4R models for Mode 1 & 3.

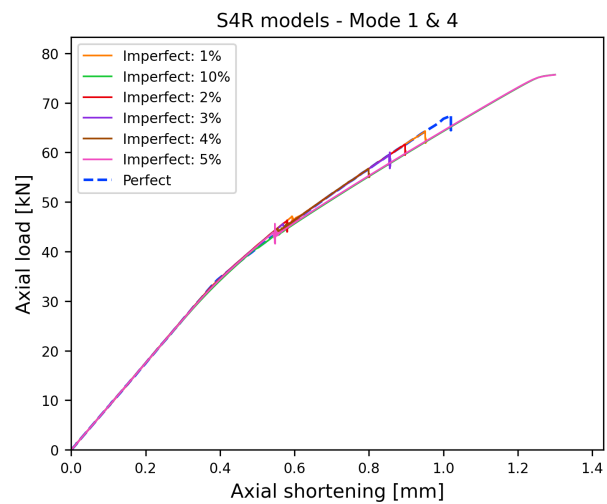


Figure B.2: S4R models for Mode 1 & 4.

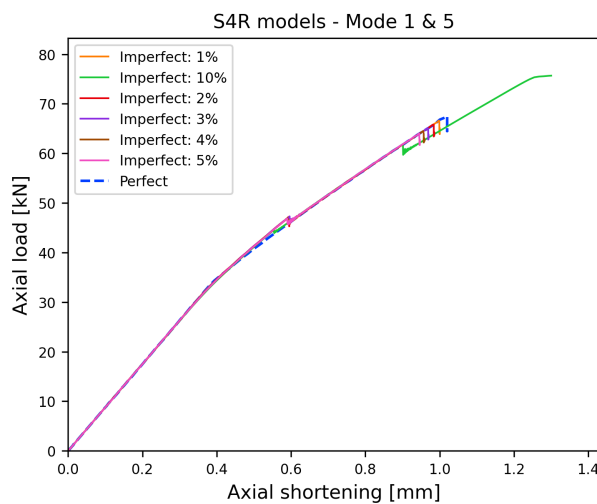


Figure B.3: S4R models for Mode 1 & 5.

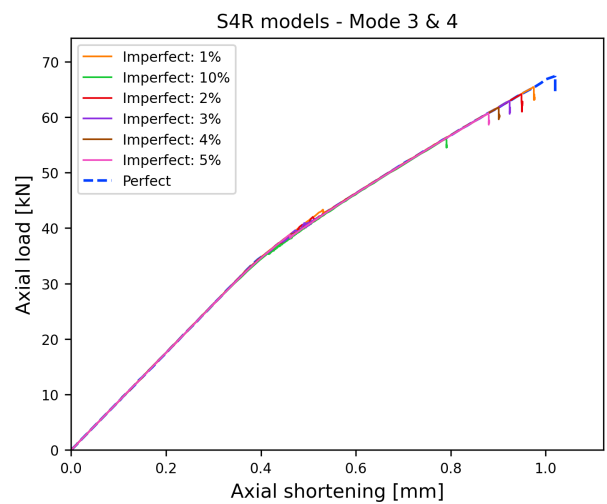


Figure B.4: S4R models for Mode 3 & 4.

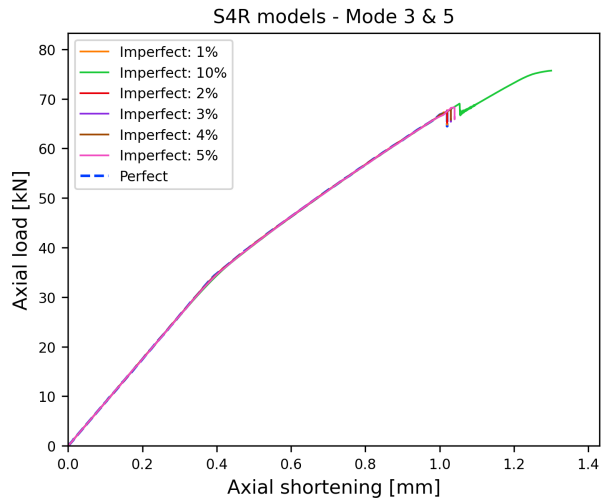


Figure B.5: S4R models for Mode 3 & 5.

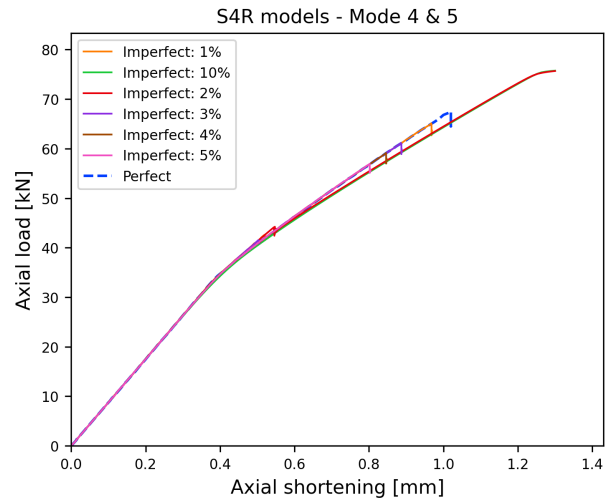
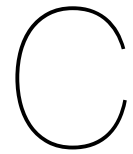


Figure B.6: S4R models for Mode 4 & 5.



Additonal Data

Table C.1: Comparison of experimental data with imperfect S4R models for Mode 1 & 5.

Description	Lanzi case	FEM model (Imp: 1%)	Diff (%)	FEM model (Imp: 5%)	Diff (%)
First buckling load [kN]	32.9	33.5	1.8%	32.9	0.0%
Axial shortening at the first buckling load [mm]	0.39	0.38	2.6%	0.38	2.6%
Initial stiffness [kN/mm]	83.7	88.2	5.4%	86.6	3.4%
Ultimate load [kN]	66.7	66.6	0.2%	64.0	4.0%
Axial shortening at the ultimate load [mm]	1.17	1.0	14.5%	0.94	19.7%

Table C.2: Comparison of experimental data with imperfect S4R models for Mode 3 & 4.

Description	Lanzi case	FEM model (Imp: 1%)	Diff (%)	FEM model (Imp: 5%)	Diff (%)
First buckling load [kN]	32.9	32.5	1.2%	31.4	4.6%
Axial shortening at the first buckling load [mm]	0.39	0.37	4.9%	0.36	7.7%
Initial stiffness [kN/mm]	83.7	87.6	4.7%	87.2	4.2%
Ultimate load [kN]	66.7	65.4	2.0%	60.7	9.0%
Axial shortening at the ultimate load [mm]	1.17	0.97	16.8%	0.88	25.0%

